

Demystifying the coronal line region of active galactic nuclei: spatially resolved spectroscopy with HST

Ximena Mazzalay^{1,2*}, Alberto Rodríguez-Ardila³ and S. Komossa^{2†}

¹*Instituto de Astronomía Teórica y Experimental, CONICET-UNC, Laprida 854, X5000BGR, Córdoba, Argentina*

²*Max-Planck-Institut für extraterrestrische Physik, Postfach 1312, 85741 Garching, Germany*

³*Laboratório Nacional de Astrofísica, Rua dos Estados Unidos 154, Bairro das Nacões, CEP 37500-000, Itajubá, MG, Brazil*

ABSTRACT

We present an analysis of STIS/HST optical spectra of a sample of ten Seyfert galaxies aimed at studying the structure and physical properties of the coronal-line region (CLR). The high-spatial resolution provided by STIS allowed us to resolve the CLR and obtain key information about the kinematics of the coronal-line gas, measure directly its spatial scale, and study the mechanisms that drive the high-ionisation lines. We find CLR regions extending from just a few parsecs (~ 10 pc) up to 230 pc in radius, consistent with the bulk of the coronal lines (CLs) originating between the BLR and NLR, and extending into the NLR in the case of [Fe VII] and [Ne V] lines. The CL profiles strongly vary with the distance to the nucleus. We observed line splitting in the core of some of the galaxies. Line peak shifts, both red- and blue-shifts, typically reached 500 km s^{-1} , and even higher velocities (1000 km s^{-1}) in some of the galaxies. In general, CLs follow the same pattern of rotation curves as low-ionisation lines like [O III]. From a direct comparison between the radio and the CL emission we find that neither the strength nor the kinematics of the CLs scale in any obvious and strong way with the radio jets. Moreover, the similarity of the flux distributions and kinematics of the CLs and low-ionisation lines, the low temperatures derived for the gas, and the success of photoionisation models to reproduce, within a factor of few, the observed line ratios, point towards photoionisation as the main driving mechanism of CLs.

Key words: galaxies: active – galaxies: nuclei – galaxies: Seyfert – line: profiles – line: formation – galaxies: kinematics and dynamics

1 INTRODUCTION

Emission-line spectroscopy of Active Galactic Nuclei (AGN) provides a wealth of information on the gaseous components in galaxy cores, and has been employed since the beginning of the twentieth century (e.g., Fath 1909). It allows us to study the physical conditions, gas kinematics, metal abundances, and their redshift evolution, provides us with means of estimating black hole masses in AGN, and has enabled us to study the evolution of galaxy – black hole scaling relations out to high redshift. Apart from the classical broad-line region (BLR) at small core distances, and the extended classical narrow-line region (NLR), a subset of AGN spectra

show lines from very highly ionised atoms, known as “Coronal lines” (CLs) because they were first observed in the solar corona. These lines are collisionally excited forbidden transitions within low-lying levels of highly ionised species with ionisation potentials $IP \geq 100 \text{ eV}$. In AGNs, the CLs are emitted in the so-called coronal line region (CLR), likely located outside the bulk of the BLR, and inside the bulk of the NLR.

CLs have been detected in the optical and infrared spectra of all types of Seyfert galaxies, including type 1s, type 2s, and narrow-line Seyfert 1 galaxies (e.g., Seyfert 1943; Penston et al. 1984; Marconi et al. 1994; Nagao, Taniguchi & Murayama 2000; Sturm et al. 2002; Rodríguez-Ardila et al. 2002, 2006; Deo et al. 2007; Mullaney & Ward 2008; Komossa et al. 2008; Gelbord, Mullaney & Ward 2009) and also radio galaxies (e.g., Best, Röttgering & Lehnert 1999; Holt, Tadhunter & Morganti 2006), and represent one of the key gaseous components of the active nucleus. They appear to be approximately equally abundant in type 1 and type 2 AGN (Rodríguez-Ardila et al., in prep).

Since the mid 70s, some evidence has been reported that

* E-mail: ximena@mpe.mpg.de (XM); aardila@lna.br (ARA); skomossa@mpe.mpg.de (SK)

† Based on observations made with the NASA/ESA Hubble Space Telescope, obtained from the data archive at the Space Telescope Science Institute. STScI is operated by the Association of Universities for Research in Astronomy, Inc. under NASA contract NAS 5-26555.

optical CLs tend to be broader than low-ionisation forbidden lines (Phillips & Osterbrock 1975; Cooke et al. 1976) and that their centroid position is blueshifted with respect to the systemic velocity of the galaxy (Grandi 1978; Penston et al. 1984). This has been interpreted as evidence for a location of the CLR closer to central engine than the classical NLR and probably associated with outflows (e.g., Ward & Morris 1984; Mullaney et al. 2009). Consistent with this scenario is the correlation found between the ionisation potential necessary to create the ionised species and the line width, seen in some (but not in all) Seyfert galaxies (Wilson 1979; Pelat, Alloin & Fosbury 1981; Evans 1988; Erkens, Appenzeller & Wagner 1997).

So far, the precise nature and origin of CLs remained uncertain. Several models have been considered in explaining the CLs, including winds from the molecular torus (e.g., Pier & Voit 1995; Nagao et al. 2000; Mullaney et al. 2009), an origin within the (X-ray) ionised absorbers (e.g., Komossa & Fink 1997a, b; Porquet et al. 1999), a high-ionisation component of the inner NLR (e.g., Komossa & Schulz 1997; Ferguson, Korista & Ferland 1997b; Binette et al. 1997), and a low-density component of the ISM (Korista & Ferland 1989).

In most observational studies, the CLs are not directly spatially resolved, due to the fact that the CLR is more compact than the classical NLR. One indirect way to obtain spatial information is by variability studies. Very few galaxies have ever shown dramatic variability of their CLs [IC 3599 (Brandt, Pounds & Fink 1995; Grupe et al. 1995; Komossa & Bade 1999) and SDSSJ0952+2143 (Komossa et al. 2009)], likely a response to a rare high-amplitude outburst in the ionising radiation from a temporary accretion event. Mild CL variability is occasionally seen (e.g., Netzer 1974; Veilleux 1988), but as a class, CLs do not vary very much at all (Veilleux 1988).

A more direct way to resolve the CLR has become possible only recently by means of Hubble Space Telescope (HST) and ground-based integral-field spectroscopy. Recent advances in the understanding of the CLR include the determination of the size and morphology of high-ionisation gas by means of infrared HST and ground-based AO infrared imaging/spectroscopy in a few objects (e.g., Thompson et al. 2001; Prieto, Marco & Gallimore 2005; Sánchez et al. 2006; Riffel et al. 2008; Bedregal et al. 2009; Storchi-Bergmann et al. 2009). The results indicate CLR with sizes varying from compact (~ 30 pc) to extended (~ 200 pc) and the CLR is aligned preferentially with the direction of the lower ionisation cones seen in these sources. Moreover, the most highly ionised species show the smallest sizes of the emitting regions. In the optical regime, HST spectroscopy was employed to study spatially resolved emission-line ratios of nearby Seyfert galaxies, including in the measurements and models the lowest-ionisation coronal lines [Ne V] and [Fe VII] (e.g., Nelson et al. 2000; Kraemer & Crenshaw 2000a; Kraemer et al. 2000; Whittle et al. 2005; Collins et al. 2005, 2009).

The study of CLs is important for several reasons. Firstly, CLs with their high-ionisation potentials trace an important part of the ionising continuum in the EUV to soft X-ray regime, which is not always directly accessible from observations. Secondly, the CL [Ne V] λ 3426 is often the only forbidden line identified in high-redshift spectra of AGN and is therefore used to identify AGN in deep and wide

multi-wavelength surveys. In the future, the line properties (flux and profile) may be further used as a diagnostic of the AGN properties, potentially including a measurement of host galaxy velocity dispersion. A better understanding of the site and conditions of formation of this line is therefore of great interest. In several galaxies, there is strong evidence that the bulk of the CLR is in outflow (e.g., Erkens et al. 1997; Mullaney et al. 2009). If this is a global property of CLRs in all AGN, their study provides us with new constraints on the formation and driving mechanism (e.g., radiation pressure versus lateral flows around nuclear radio jets) of such outflows in the very cores of AGN. Observations of high-spatial resolution are thus essential in spatially resolving the scales close to where these outflows might form. The widths, profiles, and wavelength shifts of the CLs constitute important diagnostics of these energetic processes (such as outflows, or also shocks) in regions close to the central engine.

Given that most previous CLR studies were based on seeing-limited ground-based spectroscopy, key to making further progress in understanding the CLR, and to testing CLR models is spatially resolved spectroscopy, which directly zooms into the central tenths of parsecs of the nearby Seyfert galaxies. The highest possible spatial resolution to date can only be achieved with observations above the atmosphere, as they are possible with the HST. Here, we present Space Telescope Imaging Spectrograph (STIS) optical spectroscopy of a selected sample of local AGNs with the goals of studying the structure and physical properties of the CLR. The spectra, described in Section 2, allow us for the first time the simultaneous study of coronal lines with $100 < IP < 504$ eV in a spatially resolved fashion. Questions that we will address are the extent of the CLR (Section 3), its kinematics and how it compares to that of the low-ionisation gas (Section 4), and the role of shocks and photoionisation in determining the strengths of CLs (Section 5). The main conclusions of this work are summarised in Section 6.

2 SAMPLE SELECTION, OBSERVATIONS, AND DATA REDUCTION

We retrieved archival optical HST/STIS spectra of 10 Seyfert galaxies listed in column 1 of Table 1. The original sample was composed of 101 Seyfert galaxies observed with STIS and published by Spinelli et al. (2006). Our selection was based on two criteria: first, we chose galaxies with previous coronal line detections and second, we restricted the sample to relatively nearby objects ($z < 0.018$) in order to obtain high-spatial resolution in physical scales. In all cases, the detector consisted of a 1024 x 1024 CCD with a spatial scale of 0.051 arcsec/pixel, giving spatial resolutions ranging from 3 to 17 pc (for an assumed value of $H_0 = 75 \text{ km s}^{-1} \text{ Mpc}^{-1}$).

Since the galaxies of our sample were observed in different STIS observing programs, the spectra were obtained in different instrumental configurations. In Table 2 we present a log of these observations. The spectral region around the H β emission line was covered by the G430L grating (2900–5700 Å, hereafter blue spectra), with a spectral resolution of 2.73 Å/pix. When available, the region around the H α emission line was covered either by the G750L (5250–10300 Å) or

Table 1. Properties of the galaxies in the sample.

Object	Seyfert Type	z	Scale [pc arcsec ⁻¹]
Mrk 3	Sy2	0.01350	260
Mrk 348	Sy2	0.01503	290
Mrk 573	Sy2	0.01717	330
NGC 1068	Sy2	0.00379	73
NGC 3081	Sy2	0.00797	155
NGC 3227	Sy1.5	0.00385	75
NGC 4151	Sy1.5	0.00331	65
NGC 4507	Sy1.9	0.01180	230
NGC 5643	Sy2	0.00399	77
NGC 7682	Sy2	0.01714	330

the G750M (6300–6850 Å) grating (hereafter red spectra), with spectral resolutions of 4.92 Å/pix and 0.56 Å/pix, respectively.

The retrieved 2D spectra were already rectified and wavelength and flux calibrated. The images were converted from surface brightness per Angstrom (in erg cm⁻² sec⁻¹ Å⁻¹ arcsec⁻²) to flux per Angstrom (in erg cm⁻² sec⁻¹ Å⁻¹) following the procedure described in section 5.4.1 of the STIS Data Handbook¹. Some of the galaxies included multiple exposures, dithering the target along the slit (see Table 2). We shifted and combined these images using the `imshift` and `imcombine` tasks of IRAF, respectively.

One-dimensional (1D) spectra along the spatial direction were extracted from the 2D frames for each object using the IRAF task `apall`. The nuclear spectra, centred at the peak of the continuum flux, were obtained by summing up the signal in a window size of 0.204'' (4 pixels). In addition, several extractions in an aperture window 0.102'' (2 pixels) long were done consecutively at both sides of the nucleus in the spatial direction. The number of extractions varied from object to object depending on the extent of the coronal line emission and other lines of the NLR.

The flux, full width at half maximum (FWHM), and peak position of the coronal lines [Ne v]λ3425, [Fe vii]λ3586, [Fe vii]λ3760, [Fe xiv]λ5303, [Fe vii]λ6086, [Fe x]λ6374, [S xii]λ7611, and [Fe xi]λ7892 were measured in each spectrum, if detected in the first place. If the region containing [Fe vii]λ6086 was available for a given galaxy, measurements on that line were preferred over [Fe vii]λ3586 and [Fe vii]λ3760 because the former is significantly stronger than the latter two. For comparison purposes, the low- and mid-ionisation lines [O ii]λ3727, [Ne iii]λ3869, and [O iii]λ5007 were also measured. In order to make an accurate subtraction of the continuum, we have selected continuum regions approximately 300–600 km s⁻¹ away from the lines under consideration. For most targets we found that a straight line approximated the AGN continuum well, while in some sources (those with the highest signal-to-noise ratios) the continuum was fit with a power law. After subtraction of the interpolated continuum, it was assumed that the observed profile is well represented by a single or a sum of Gaussian components. The LINER routine (Pogge & Owen 1993) was used in this process. Overall,

this approach was adequate for all spectra. Note that the spectra presented here are convolved with the STIS point-spread function (PSF). Although the STIS PSF for the CCD modes is narrow (FWHM = 2.3 pixels at 7750 Å), some contamination from the bright nuclear source to the extended regions is possible (see Nelson et al. 2000 for a detailed discussion of NGC 4151). We have analysed the PSF profile along the cross-dispersion axis, as traced by the point-like continuum emission of NGC 4151, and compared it to the spatial distribution of the different lines measured in the spectra presented here. We found that the PSF shape is much steeper than the slowly declining profile of the lines measured in the Seyfert 2 galaxies and therefore, contamination by the central brightest regions to the extended emission is negligible. Cecil et al. (2002) and Kraemer & Crenshaw (2000a) reached a similar conclusion in the case of NGC 1068. However, the particular case of NGC 4151 is more complicated due to its very bright nucleus. While emission in the wings of the PSF contributes to the measurements next to the nucleus (up to 70%), further out this contribution is of only a few percent (less than 30%) and does not affect significantly our results. Throughout this paper, we report the directly measured FWHMs of emission lines, rather than performing any instrumental correction, because the actual corrections depend significantly on the spatial extent of the emission region, and are different for point sources and extended sources (STIS Instrument Handbook¹); and because at any given location, emission from extended and point-like regions might contribute to the emission-line profile. In Table 2 we report the spectral resolution under the assumption of point-like emission. These values were calculated taking into account the spectral resolution (FWHM in pixels) of the 0.1'' and 0.2'' slits for point sources and the spectral resolution provided by the different gratings. For extended sources, the instrumental FWHM can be of the order of 2–3 times greater than for point-like sources.

The velocity field along the slit, FWHMs and flux distributions of the lines of interest in the spatial direction were constructed for the objects of the sample. Because of the non-uniformity of the data, mostly when combining data gathered with the gratings G430L and G750M, only flux and centroid positions for the lines covered by the latter grating were employed. The measured flux uncertainties are typically about 10%, with some degradation in fainter regions (< 30%). However, as discussed above, at some distances from the nucleus of NGC 4151, the reported values are overestimated due to PSF effects, and we therefore consider a typical upper limit of 30% for the overestimation of any reported line fluxes. In general, line centroids and FWHMs have errors of less than 150 km s⁻¹. These errors were estimated using the standard deviation of five different measurements of the lines made with different continuum selections. However, the errors in the FWHM resulting from uncertainties in the spatial extent of the emission region (mentioned above) are much larger than this. We nevertheless report FWHMs, because one can still identify systematic trends in FWHM changes, identify local abrupt changes, and compare FWHMs of lines of different degree of ionization.

¹ <http://www.stsci.edu/hst/stis/documents/handbooks/>

Table 2. Observation log

Object	Dataset	Slit Width [arcsec]	Grating	PA [°]	Spectral Res. [km s ⁻¹]	Spatial Res. [pc pix ⁻¹]
Mrk 3	O5KS01010	0.1	G430L	-108	250	13
"	O5KS01020	0.1	G750L	-108	350	"
Mrk 348	O5G405020	0.2	G430L	146	270	15
Mrk 573	O6BU02050	0.2	G430L	-71	270	17
"	O6BU02040	"	"	"	"	"
"	O6BU02020	0.2	G750M	-71	40	"
"	O6BU02010	"	"	"	"	"
"	O6BU02030	"	"	"	"	"
NGC 1068	O4WK010A0	0.1	G430L	202	250	4
"	O4WK010B0	0.1	G750L	202	350	"
NGC 3081	O6BU06040	0.2	G430L	-110	270	8
"	O6BU06050	"	"	"	"	"
"	O6BU06030	0.2	G750M	-110	40	"
"	O6BU06010	"	"	"	"	"
"	O6BU06020	"	"	"	"	"
NGC 3227	O5KP01020	0.2	G430L	-150	270	4
"	O5KP01040	0.2	G750L	-150	370	"
NGC 4151	O42302070	0.1	G430L	221	250	3
"	O42303050	"	"	"	"	"
"	O42302080	0.1	G750L	221	350	"
"	O42303060	"	"	"	"	"
"	O42305050	0.1	G430L	70	250	3
"	O42304090	"	"	"	"	"
"	O42305060	0.1	G750L	70	350	"
"	O423040a0	"	"	"	"	"
NGC 4507	O5DF03010	0.2	G430L	-34	270	12
"	O6BU17020	0.2	G750M	-138	40	"
"	O6BU17010	"	"	"	"	"
NGC 5643	O6BU11040	0.2	G430L	-127	270	4
"	O6BU11050	"	"	"	"	"
"	O6BU11010	0.2	G750M	-127	40	"
"	O6BU11020	"	"	"	"	"
"	O6BU11030	"	"	"	"	"
NGC 7682	O6BU14040	0.2	G430L	18	270	15
"	O6BU14050	"	"	"	"	"
"	O6BU14010	0.2	G750M	18	40	"
"	O6BU14020	"	"	"	"	"
"	O6BU14030	"	"	"	"	"

3 RESULTS

In this section we will describe the general properties of the galaxies in the sample and the main results obtained from the measurements of the line fluxes for each galaxy. Emphasis is on the extent of the CLR and how its extent compares with gas of lower ionisation. To this purpose, we have plotted the flux distributions of the high-ionisation lines measured for the galaxies Mrk 573 (Fig. 1), NGC 1068 (Fig. 3), Mrk 3 (Fig. 4), NGC 4151 (Fig. 5 and 6), NGC 4507 (Fig. 7), and NGC 3081 (Fig. 9). We also added to the plots the flux distribution of the low-ionisation lines [Ne III], [O III], and [O II] for comparison. Additionally, Table 3 shows the line fluxes measured at different distances from the nucleus for the remaining galaxies in the sample, NGC 3227, Mrk 348, NGC 5643, and NGC 7682. Table 4 shows the spatial extent to which each coronal line is detected as well as the total extent of the [O III] line emission along the slit. Notice that, unless stated otherwise, these extents correspond to the last position where the S/N was high enough for the line of interest to be detected (at 3σ level). The possible presence of

line emission further out from the nucleus was checked in two ways: first, we extracted additional spectra by summing up the signal from several pixels (up to 10) adjacent to the last spectrum where the line was detected. In all cases we found no emission further out. Second, we used the upper limit of the fluxes of the lines of interest (derived from the continuum rms at the position where these lines should be located and an assumed FWHM) to compute line ratios involving the coronal line and a lower ionisation line present in the spectrum (e.g. [Ne v]/[O III], [Fe VII]/[O III], [Fe X]/[O I]), and compared them with those measured closer to the nucleus. In most cases, these upper limits are of the order or slightly lower than the line ratios measured closer to the nucleus. Therefore, although we can not discard emission further out, if there is any, it is very weak. Also notice that the distances reported in this work can be affected by projection effects, for which we did not correct. For these reasons, the extents given in Table 4 should be taken as lower limits.

3.1 Mrk 573

This barred Seyfert 2 galaxy displays a very rich coronal line spectrum, from optical to near-infrared wavelengths (e.g., Koski 1978; Tsvetanov & Walsh 1992; Storchi-Bergmann et al. 1996; Riffel, Rodríguez-Ardila & Pastoriza 2006; Mullaney & Ward 2008). Recently, Ramos Almeida et al. (2008) proposed that Mrk 573 is, in fact, a narrow-line Seyfert 1 galaxy (NLS1) rather than a Seyfert 2 based on the observations of O I and Fe II permitted lines in the near-infrared. These features are characteristics of only type 1 galaxies, as they are produced in the BLR. Nagao et al. (2004) reported spectropolarimetric observations of the NLR of this source and found that it shows not only scattered broad H α emission but also various narrow forbidden emission lines. The degree of polarisation of the latter features is positively correlated with the ionisation potential of the corresponding ion and the critical density of the corresponding transition. They attributed these correlations to obscuration of the stratified NLR by the geometrically and optically thick dusty torus.

The HST/STIS spectra of this galaxy were obtained with the slit oriented at a PA of -71° , that is, nearly aligned to both the [O III] ionisation cone (PA= 120°) reported by Regan & Mulchaey (1999) and to the radio jet, whose NW component lies at PA= -51° (Nagar et al. 1999). Previous reports pointed out that the [O III] emission is extended along the same direction as the radio emission (Haniff, Wilson & Ward 1988; Pogge & De Robertis 1995). The blue nuclear spectrum reveals strong coronal lines of [Ne V], [Fe VII], and [Fe XIV], in addition to forbidden low- and medium-ionisation lines of [O II], [Ne III], and [O III], as well as recombination lines of H I and He II. The red spectra display [Fe X], along with low-ionisation lines of [O I], [N II] and [S II], as well as H α . Previous studies using HST data (Ferruit et al. 1999; Quillen et al. 1999; Schlesinger et al. 2009) have shown that the low- to medium-ionisation gas is extended to distances of up to ~ 1100 pc to the SE and ~ 1500 pc to the NW. In addition, the circumnuclear region is rich in bright arcs and knots of emission-line gas strongly aligned and interacting with a kiloparsec-scale low-power radio outflow (Pogge & De Robertis 1993; Falcke, Wilson & Simpson 1998; Ferruit et al. 1999). Because all coronal lines we detected in this object are restricted to the inner 200 pc, that is, strictly at smaller scales than the region where the arcs and bright knots are located, we concentrate our attention only on the coronal features and discard any association between the arcs and knots and the high-ionisation lines.

A close look at Fig. 1 shows that the CLR tends to be slightly more extended towards the NW than to the SE. Moreover, the [O III] emission displays two small bumps at ~ 120 pc and ~ 250 pc NW, not observed in the high-ionisation gas. To the SE, the extended emission drops more smoothly. [Ne V] is the most extended CL, observed out to ~ 160 pc NW and 120 pc SE from the nucleus (see Table 4). [Fe VII] $\lambda 3586$, in contrast, is detected only up to 50 pc SE. To the NW, it is restricted to the unresolved nucleus. However, it should be kept in mind that the true extent of the [Fe VII] gas may be larger. Unfortunately, the only [Fe VII] line covered by the spectra is in the blue region, where it is only a small fraction of [Fe VII] $\lambda 6086$, the strongest Fe $^{+6}$ line in the optical. For this reason, the true spatial extent

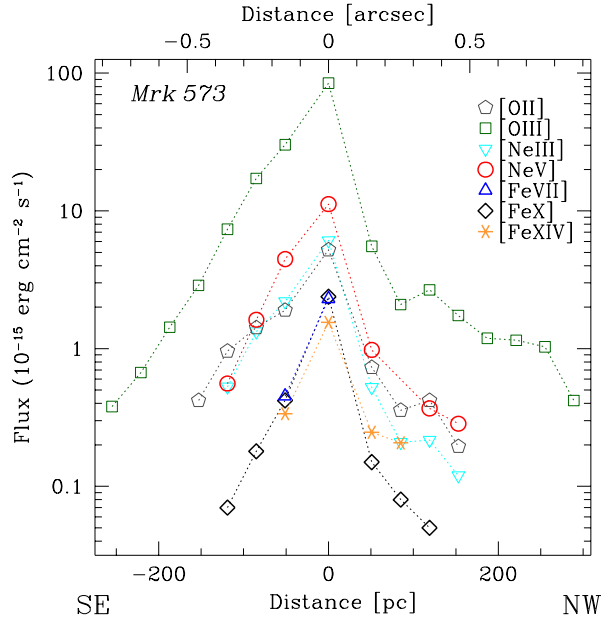


Figure 1. Flux of the principal emission lines measured for Mrk 573 as a function of the projected distance to the nucleus. Typical error bars have the size of the symbols (see Section 2) and are therefore not shown.

of [Fe VII] is inconclusive. In fact, Storchi-Bergmann et al. (1996) presented high signal-to-noise spectra of Mrk 573 and reported the detection of [Fe VII] $\lambda 6086$ and [Ne V] $\lambda 3425$ at a distance of $6''$ NW and SE from the nucleus. [Fe VII] $\lambda 3586$ was not reported.

The blue spectra also include [Fe XIV] $\lambda 5303$, the highest ionisation line in the optical region detected in Mrk 573. It is observed in the unresolved nuclear spectrum and its emission extends ~ 80 pc to the NW and ~ 50 pc to the SE.

The red spectrum, which has a better spectral resolution than the blue ones, contains [Fe X] $\lambda 6374$. This line is prominent in the nucleus, displaying a conspicuous broad flat top profile (see Fig. 2) typical of a double-peaked structure, in contrast to the Gaussian-like profile seen in [O I] and [S II]. The double-peaked nature of [Fe X], firstly recognised by Schlesinger et al. (2009) in the nuclear spectrum of Mrk 573, became evident when we examined the line profile in the different apertures, shown in Fig. 2. It can be seen that the blue peak becomes progressively more prominent than the red one from the NW to the SE except at $0.15''$ SE, where its intensity, relative to the red peak, decreases. Moreover, the relative separation between both peaks increases: while in the nuclear aperture they are separated by ~ 180 km s $^{-1}$, at $0.36''$ SE, the last position where [Fe X] is detected, they are separated by ~ 350 km s $^{-1}$. From Fig. 2 it is also easy to see that [Fe X] extends up to 120 pc both NW and SE. For comparison, [O I] is detected up to 150 pc SE and 190 pc NW (these apertures are not shown in the plot). However, there are positions ($0.36''$ NW, $0.25''$ NW, and $0.36''$ SE) where no [O I] emission is seen. Moreover, the profiles of the other lines seem rather different from that of [Fe X], leading us to suggest that this emission should be related to a high-ionisation matted-bounded cloud that has been radially accelerated. It is worth to mention that at 85 pc SE, the line profiles of H α ,

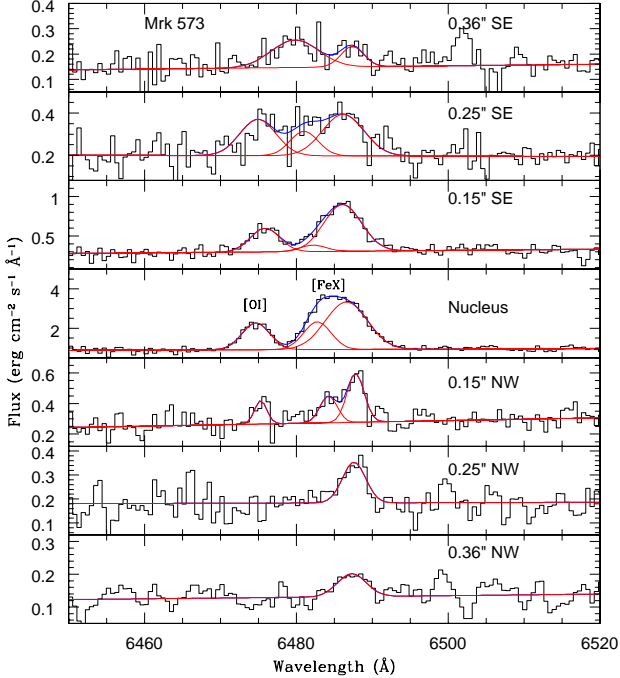


Figure 2. [O I] and [Fe X] profile fitting for the nucleus and adjacent regions of Mrk 573.

[N II], and [S II] are very complex, with multiple components in each line while that of [Fe X] is dominated by the red peak.

The increase in relative separation between the red and blue peaks of [Fe X] with the distance when going from NW to SE is unique. To the best of our knowledge no previous report of such a behaviour in an optical emission line with $IP > 200$ eV is found in the literature. Moreover, the detection of [Fe X] to distances of up to 120 pc, which we report here, is remarkable, and puts tight constraints on photoionisation models. This issue will be examined in more detail in Section 5.2.2.

3.2 NGC 1068

NGC 1068 is one of the nearest Seyfert galaxies and is usually considered as the archetypal Seyfert 2 galaxy. It has been extensively studied in every wavelength range, from X-rays to the radio regime (e.g., Oliva & Moorwood 1990; Miller, Goodrich & Mathews 1991; Antonucci, Hurt & Miller 1994; Machetto et al. 1994; Gallimore et al. 1996; Young et al. 1995; Marconi et al. 1996; Young, Wilson & Shopbell 2001; Kinkhabwala et al. 2002; Jaffe et al. 2004). The structure of the inner regions of this galaxy is extremely complex. It is classified as a (R)SA(rs)b galaxy, showing a strong and large inner bar inside a very large, weak outer bar/oval disk. A cone-like NLR oriented roughly in the northeast-southwest direction was resolved into filaments and point sources by HST narrow band imaging (Evans et al. 1991; Macchetto et al. 1994). Spatially coincident with the NLR, VLA maps revealed a $13''$ radio bipolar structure constituted by jets ending in radio lobes along the $PA = 30^\circ$ (Wilson & Ulvestad 1983). On sub-arcsecond scales, the jet is resolved into four components (Gallimore et al. 1996). Two of these

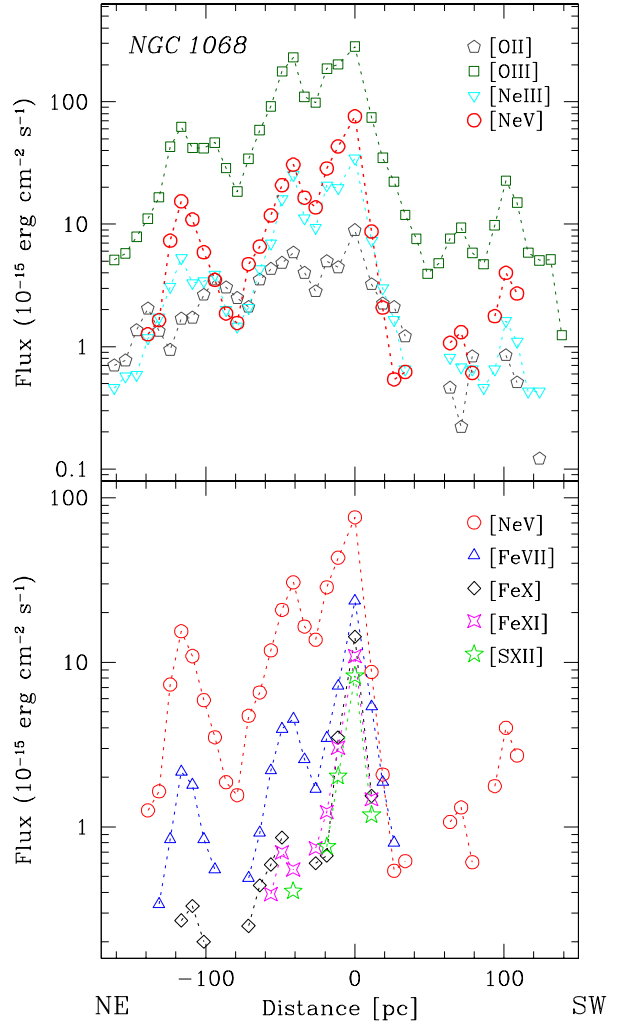


Figure 3. Flux of the principal emission lines of NGC 1068 as a function of the projected distance to the nucleus. For visualisation purposes we plotted the line flux distributions in two panels: in the upper panel we show [Ne V] and low-ionisation lines and in the lower panel [Ne V] and high-ionisation lines. Typical error bars have the size of the symbols (see Section 2).

components are located roughly in the north-south direction. The component located more to the north is believed to be the hidden active nucleus. At a distance of $\sim 0.3''$ from it, towards the north (along the $PA = 10^\circ$), the third component is located. Here, the jet seems to have an abrupt change in direction and the fourth component is observed at a distance of $\sim 0.3''$ from the third along the $PA = 30^\circ$. NGC 1068 is also a strong source of X-ray emission. Chandra high-resolution images showed an impressive agreement between the X-ray emission and the [O III] images on small and large scales, with a detailed correspondence between both (Young et al. 2001). These images showed a bright nucleus, extended bright emission toward the NE, and large scale structure reaching at least 1 arcmin to the NE and SW.

The complexity of this galaxy is also evident in the line profiles and fluxes, showing strong variations between adjacent spectra along the slit (see Fig. 3). Notice that the STIS

slit was located along the ionisation cone and roughly coincident with the nuclear radio jet (see Table 2). The STIS spectra show several coronal lines in the 2900–10300 Å range, from [Ne v] and [Fe VII] lines, whose ionisation potential are ~ 100 eV, to the extreme ionisation [S XII]λ7611 line, with an ionisation potential of 504.7 eV. This very high-ionisation line has been reported only in NGC 1068 (Kraemer & Crenshaw 2000b).

The most extended CLs, [Ne v]λ3425 and [Fe VII]λ6086, exhibit similar spatial morphology as the intense [O III]λ5007 line, showing several blobs located mainly in the NE side of the nucleus. The [Ne v] line extends up to 140 pc NE, with two peaks of emission located at 40 pc and 115 pc NE of the nucleus. Towards the SW this line is relatively weak and vanishes and re-appears several times. The maximum extent towards the SW is 110 pc. The [Fe VII]λ6086 line is observed up to 130 pc NE of the nucleus, though it is not detected from 80 pc to 85 pc. At the SW side, this line is much less extended, observed only up to 25 pc. At ~ 20 pc NE enhanced emission is observed in the low-ionisation lines plotted in Fig. 3. This blob is not followed by the high-ionisation lines.

The [Fe X]λ6374 line is more complicated to analyse due to the strong blend with the [O I]λ6363 line. However, fixing the parameters (FWHM, centroid position, and intensity) of the latter, as determined by the near [O I]λ6300 line, which belong to the same doublet, allowed us to measure the size of the [Fe X] emission region. Towards the SW this line is observed only next to the nucleus, at 10 pc. On the other hand, the extent towards the NE is quiet large, extending almost as much as the [Fe VII] line. It is clearly present next to the nucleus (10 pc NE), from 50 pc to 65 pc, and from 110 pc to 115 pc. The higher ionisation regions, traced by [Fe XI]λ7892 and [S XII]λ7611 lines, are much more compact but still spatially resolved. These lines extend up to ~ 10 pc to the SW, and towards the NE up to 50 pc and 20 pc, respectively. In general, when the high-ionisation lines are observed, they tend to follow the same flux distribution as the lower ionisation lines (i.e. [O III]).

It is interesting to note that, towards the NE, the size of the extended emission decreases as the ionisation potential of the “coronal ions” increases, in complete agreement with photoionisation by a central source. However, towards the SW the lines show an entirely different behaviour that cannot be explained simply by anisotropy of the ionising radiation. Although [Ne v]λ3425 and [Fe VII]λ6086 have almost the same ionisation potential and critical densities, the first one extends much more towards the SW than the second one. Similar results have been found in the NIR. Geballe et al. (2009) reported *L*– and *M*–band spectroscopy of the nucleus of NGC 1068 obtained at 0.3″ (20 pc) resolution with the spectrograph slit aligned approximately along the ionisation cones of the AGN. They found that all CLs detected in that wavelength region peak 20 pc north of the AGN and are very weak or not present towards the south. This can be understood in terms of the strong extinction towards the SW measured in this object. Assuming a case B recombination ratio of $H\alpha/H\beta = 3.1$ (Osterbrock 1989) we determined the reddening as a function of the distance to the nucleus. Towards the NE the measured ratio is close to the theoretical ratio, therefore reddening is not strongly affecting the gas. However, towards the SW the reddening

increases with the distance up to $E(V-B) = 0.9$ measured at 35 pc SW. Further out, no determination of the reddening was possible due to the weakness of the hydrogen lines. Assuming that in the absence of reddening the values of the ratio [Ne v]λ3425/[Fe VII]λ6086 towards the SW are similar to the ones measured to the NE, [Ne v]λ3425 is, intrinsically, at least 10 times stronger than [Fe VII]λ6086. Clearly, the dusty environment to the SW extinguishes completely the latter line.

The [Fe VII] 3759/6086 and 5159/6086 Å line ratios can be use as diagnostics of the density in the Fe^{+6} emitting region (Keenan & Norrington 1987). Of all the galaxies in the sample, NGC 1068 is the only one for which these lines are available. However, due to the weakness of the lines in the blue spectra and the uncertainties due to reddening corrections (specially in the case of the former ratio which is strongly sensitive to extinction), we were not able to derive a reliable value for the density of the coronal-line gas.

3.3 Mrk 3

Mrk 3 is a nearby S0 galaxy. Although it is classified as a Seyfert 2 galaxy from optical spectroscopy, it shows evidence of a hidden Seyfert 1 nucleus in polarised light (Miller & Goodrich 1990). The morphology of the inner regions of Mrk 3 is highly intricate. Narrow band HST imaging, centred at [O II]λ3727, [O III]λ5007, $H\gamma$, and $H\alpha$, showed an S-shaped NLR extending across the inner 2″ in the east-west direction ($PA = 70^\circ$ east of north) and composed of a large number of resolved knots (Capetti et al. 1995). This small scale structure is embedded in a more extended (10″) bi-conical emission region aligned along $PA = 114^\circ$ (Pogge & De Robertis 1993). Moreover, high resolution radio observations revealed two highly collimated radio jets lying along $PA = 84^\circ$ (Kukula et al. 1993). The jet shows a slight S-shape curvature expanding about 2″, the west side ends in an extended lobe containing a hot spot at 1.2″ from the nucleus. The soft X-ray emission of Mrk 3 is also spatially elongated along the [O III] emission (Sako et al. 2000).

Two different gratings were used in the STIS observations of Mrk 3 (G430L and G750L), with the slit following the S-shaped NLR at $PA = 73^\circ$ (see Table 2) and nearly aligned with the radio jet. An inspection of the optical spectrum of this galaxy shows that it displays very weak coronal line emission. Indeed, in the blue region, only [Ne v]λλ3343,3425 and faint [Fe VII]λ5158 are observed. In the red spectra, [Fe VII]λ5722 and λ6086 are detected. Higher ionisation lines are not present in the optical spectrum of Mrk 3 and, to our knowledge, neither in the infrared region (Osterbrock, Shaw & Veilleux 1990; Wilson & Nath 1990; Heisler & De Robertis 1999; Knop et al. 2001). This makes Mrk 3 one of the lowest ionisation galaxies of the whole sample. Interestingly, Mrk 3 exhibits the most extended CLR of the ten AGN studied here (see Table 4). The [Ne v]λ3425 emission, for instance, extends up to 230 pc to the SW from the nucleus and 150 pc to the NE. Moreover, [Fe VII]λ6086 can be traced up to 200 pc to the SW and 90 pc to the NE. In contrast, medium ionisation lines such as [O III]λ5007 extend up to 650 pc SW and 450 pc NE.

Similar to other lines, [Ne v]λ3425 and [Fe VII]λ6086 are stronger towards the SW, both displaying a second peak of emission which does not coincide spatially: 150 pc from the

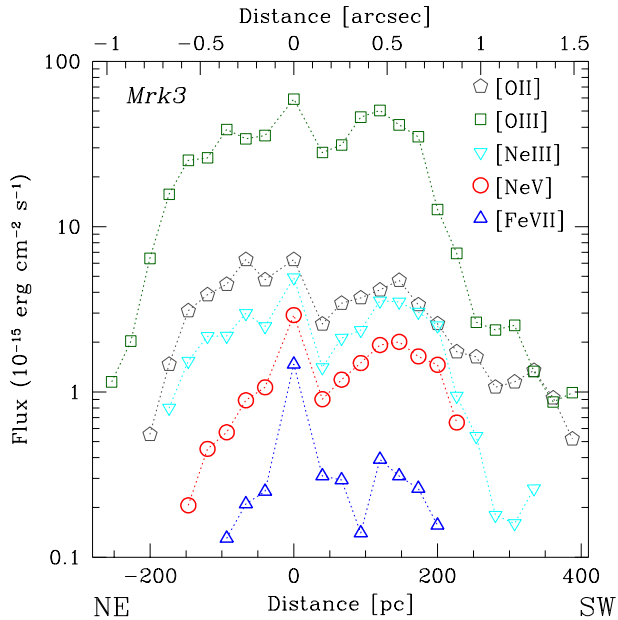


Figure 4. Same as Fig. 1, but for Mrk 3.

centre for the former and 120 pc for the latter. The flux distribution for the most conspicuous lines, including the coronal lines plotted in Fig. 4, shows a similar pattern for the five species studied.

The lack of highly ionised species in the optical spectrum contrasts to what is observed at high energies. The observed soft X-ray spectrum of Mrk 3, for instance, is dominated by line emission from highly ionised stages of the lighter metals (Pounds & Page 2005). These authors stress the similarity between the X-ray line spectrum of this object and that of NGC 1068 but recall that the fluxes are an order of magnitude less, mainly due to Mrk 3 lying at a greater distance and the attenuation at the longer wavelengths by the relatively large Galactic column in the direction of this source. As we already saw in Section 3.2, the optical spectrum of NGC 1068 displays conspicuous high-ionisation lines, not seen in Mrk 3. This result leads us to speculate if the lack of high-ionisation lines in the optical spectrum of Mrk 3 is due to technical reasons (not enough S/N) rather than to physical reasons. In order to test this scenario we assume that, as in the X-ray region, the optical spectrum of Mrk 3 is very similar to that of NGC 1068. Then, line ratios among coronal lines should be very similar in both objects, allowing us to determine an upper limit to the flux of [Fe x] in Mrk 3. The nuclear ratio $[\text{Fe x}]/[\text{Fe VII}]$ measured in NGC 1068 is 0.60 ± 0.08 . Assuming a similar ratio in Mrk 3 and a measured line flux of $8.53 \pm 1.40 \times 10^{-16}$ erg cm $^{-2}$ s $^{-1}$ for [Fe VII], the expected upper limit for the [Fe x] flux is 5.1×10^{-16} erg cm $^{-2}$ s $^{-1}$. This flux is nearly six times the RMS (3σ) of the observed adjacent continuum so, if present, this line should have been detected. Therefore, we conclude that the lack of high-ionisation lines in Mrk 3 is intrinsic, probably due to physical reasons rather than to the low S/N.

3.4 NGC 4151

NGC 4151 is a SABab galaxy that harbours a type 1 Seyfert nucleus. It is one of best studied AGNs in the literature at all wavelengths intervals and in almost every aspect of its observed spectrum (e.g., Schulz 1995; Ulrich 2000, and references therein). Due to its proximity, the NLR can be resolved from the ground, even with telescopes without AO. Ulrich (1973) showed that the NLR extends to several arcsecs and consists of at least four distinct clouds. Pogge (1989) and Pérez et al. (1989) detected [O III] emission in ground-based images, finding it to be extended by $\sim 20''$ along PA 228°. The [O III] emission of this galaxy has a biconical morphology (Schulz 1988) along PA 55°, clearly not aligned with the radio axis at PA $\sim 77^\circ$ (Ulvestad, Wilson & Sramek 1981). The total size of the radio emission is $\sim 5.5''$ (350 pc), $3''$ along the southwest direction and $2.5''$ along the northeast. The total opening angle of the cones is 70° . Coronal lines in this object have been reported from the X-ray to optical region (e.g., Penston et al. 1984; Sturm et al. 2002; Ogle et al. 2000) but, to our knowledge, no studies have shown in detail the spatial extent and kinematics of the high-ionisation gas at scales < 100 pc, except for the recent work presented by Storchi-Bergmann et al. (2009). These authors, using AO Gemini/NIFS 3D spectroscopy, mapped NIR coronal lines, showing that the emission region of these lines were no larger than 50 pc.

The HST/STIS spectra of NGC 4151 were taken at two position angles. One position, at PA= 221° , intersecting the emission cone and passing through the nucleus. The other position, PA= 70° , was offset by $0.1''$ to the south of the nucleus and coincides with the radio jet observed in this galaxy. Because of this configuration, it allows us to fully explore the extent of the CLR and compare its size with that of other lines emitted by the NLR, and to study the effects of the jet on the high-ionisation gas.

Fig. 5 and Fig. 6 show the flux distribution of [O II], [O III], [Ne III], [Ne V], [Fe VII], and [Fe x] in the spatial direction with the slit aligned along PA= 221° and PA= 70° , respectively. Overall, the flux distributions of the CLs resemble those of the lower ionisation lines. Several peaks of emission are observed at both sides of the nucleus, making evident the knotty structure of the NLR in this object. The fluxes measured along both position angles do not show any significant difference, although the fluxes for the inner ~ 40 pc along PA= 221° are slightly higher than the ones along PA= 70° . This can be explained as a result of the offset in the position of the second slit.

In terms of the size of the coronal emission region, we found that it is restricted to the inner ~ 200 pc. The [Ne v] line is the most extended. This line is detected up to 75 pc both SW and NE along PA= 221° , and 75 pc NE and 100 pc SW along PA= 70° . The region emitting [Fe VII], in contrast, is asymmetric. Along PA= 221° it is detected up to 75 pc SW but only up to 30 pc NE, while along PA= 70° this line is more extended, reaching 70 pc NE and 95 pc SW. [Fe x] is much more compact, being limited to the inner radius of 10 pc from the centre along PA= 221° and to the nucleus and next to it towards the SW along PA= 70° .

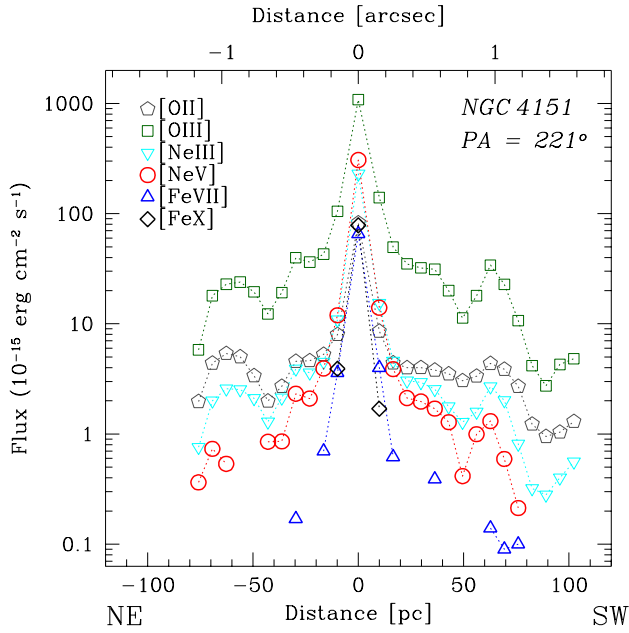


Figure 5. Same as Fig. 1, but for NGC 4151 at PA = 221°.

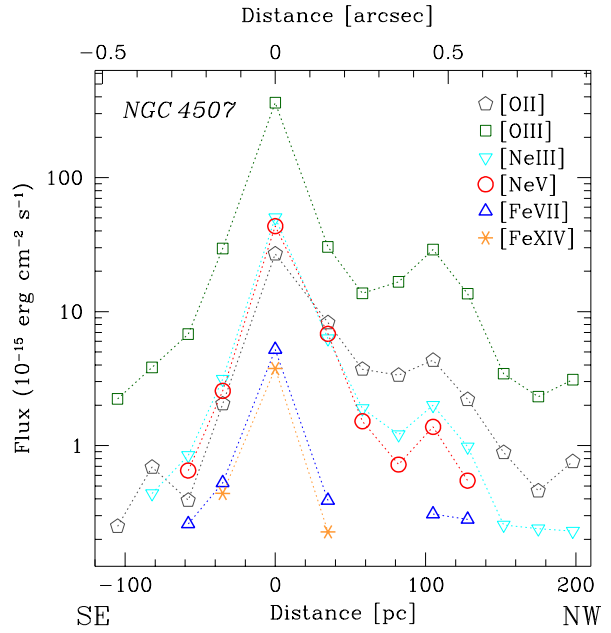


Figure 7. Same as Fig. 1, but for NGC 4507.

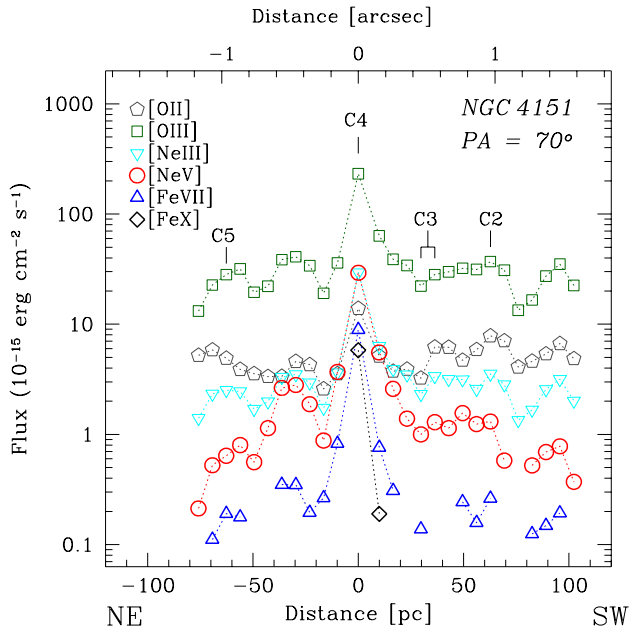


Figure 6. Same as Fig. 1, but for NGC 4151 at PA = 70°. The labels C2 to C5 indicate the position of the radio knots intersected by the slit.

3.5 NGC 4507

NGC 4507 is a barred spiral galaxy. It was originally classified as a type 2 Seyfert galaxy (Durret & Bergeron 1986) but later re-classified as Seyfert 1.9 (Veron-Cetty & Veron 1998) because of the presence of broad $H\alpha$ observed sometimes in its spectrum. Several high-ionisation lines have previously been detected in this galaxy. In the optical region [NeV], [FeVII], [FeX], [FeXI], and [FeXIV] were reported by Penston et al. (1984), Durret & Bergeron (1986), and Appen-

zeller & Östreicher (1988). In the infrared, [SiVI] 1.962 μm (Marconi et al. 1994), [SiIX] 3.94 μm (Lutz et al. 2002), and [NeV] 14.3 μm (Gorjian et al. 2007) has been detected.

The most prominent lines observed in the STIS nuclear blue spectrum of NGC 4507 are [OIII] λ 5007 and [NeIII] λ 3869, followed by the high-ionisation line [NeV] λ 3425. Other coronal lines observed are [FeVII] λ 3586, [FeVII] λ 3759, [FeVII] λ 5158, and [FeXIV] λ 5303.

Fig. 7 shows the flux variation of the most conspicuous lines versus the distance from the centre. It can be seen that the emission is asymmetric, with a strong elongation towards NW and a second peak of emission at ~ 110 pc (0.46'') from the nucleus. This second peak agrees in position with the [OIII] HST image from Schmitt et al. (2003), which shows elongated emission along PA = -35° in the inner $\sim 2''$ region and a blob of emission located at 1'' to the NW. Notice that this PA is very close to the one used in the STIS observation of the blue spectra (see Table 2). Inspection of the 2D STIS spectrum clearly shows this enhanced emission at 1'' NW (~ 230 pc) from the nucleus for the strongest lines (i.e. [OIII], $H\beta$, [NeIII], [OII]). Unfortunately we are not able to tell whether or not [NeV] is present at this distance due to the presence of a cosmic ray. [FeVII] emission is not seen at this distance from the nucleus in the STIS spectrum. Even so, this galaxy shows one of the most extended [FeVII] regions of the whole sample (as traced by the [FeVII] λ 3586 line), only exceeded by the [FeVII] λ 6086 line displayed by Mrk 3 (see Table 4). The [FeVII] region extends as much as the [NeV] λ 3425 region, reaching ~ 130 pc to the NW and ~ 60 pc to the SE. Towards the NW the [FeVII] line disappears at ~ 60 pc and is observed again at ~ 100 pc. On the other hand, the [FeXIV] emission-line gas is located closer to the nucleus. It can only be traced up to ~ 35 pc at both sides of the nucleus.

NGC 4507 was also observed at higher spectral resolution with the G750M grating. Notice however that the blue spectrum was taken with a different PA than the red spec-

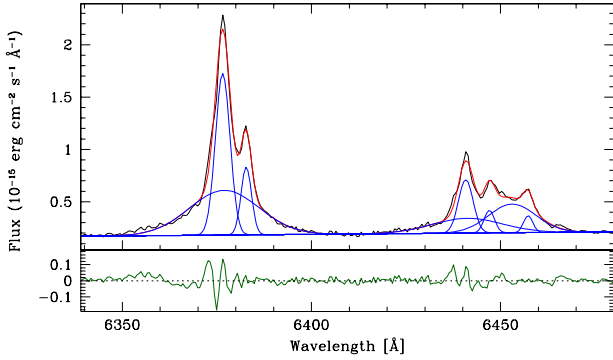


Figure 8. [O I]H6300,6363 and [Fe X] profiles of NGC 4507 decomposed into gaussian components.

tra (see Table 2). For this reason the [Fe X] line was not included in Fig. 7. The spectra show lines with very complex structures, displaying multiple components with strong variations along the slit. The [Fe X] line is strongly blended with the [O I]H6363 line. In order to deblend these lines we applied constraints in the [O I]H6363 line fitting, assuming the same FWHM, velocity shift, and 1/3 of the flux of the stronger [O I]H6300 line. The nuclear spectrum shows a very intricate [O I]+[Fe X] profile. The [O I] lines were fitted by three Gaussian components, with velocity shifts (FWHMs) of 90 km s^{-1} (200 km s^{-1}), 110 km s^{-1} (1000 km s^{-1}), and 380 km s^{-1} (150 km s^{-1}). Two Gaussian components were required to obtain a good fit of the nuclear [Fe X] line: one broad component (FWHM = 685 km s^{-1}) redshifted by $\Delta V = 155 \text{ km s}^{-1}$ and a narrow component (FWHM = 127 km s^{-1}) redshifted by $\Delta V = 352 \text{ km s}^{-1}$. The total flux in [Fe X] is $(4.8 \pm 0.3) \times 10^{-15} \text{ erg cm}^{-2} \text{ s}^{-1}$. In Fig. 8 we show the profile fitting of the [O I]-[Fe X] complex. NGC 4507 and Mrk 573 (see Section 3.1) are the only galaxies in the sample displaying such a particular [Fe X] profile. [Fe X] is also observed at both sides of the nucleus, with fluxes of $(0.26 \pm 0.13) \times 10^{-15} \text{ erg cm}^{-2} \text{ s}^{-1}$ at $\sim 35 \text{ pc}$ NW and SE.

3.6 NGC 3081

NGC 3081 is a galaxy with complex morphology showing multiple stellar and dust rings, and a weak bar, hosting a Seyfert type 2 nucleus (Buta 1990). A spectropolarimetric study by Moran et al. (2000) has established that it is a Seyfert 1, obscured by dense material at a few parsecs from the nucleus. The radio emission of this galaxy has been studied by Ulvestad & Wilson (1989). VLA observations at 6 cm and 20 cm (flux densities of 0.9 and 2.5 mJy, respectively) revealed an unresolved source.

In the optical region, in addition to strong permitted and low-ionisation forbidden lines, Appenzeller & Östreicher (1988) reported the detection of [Fe VII], [Fe X], [Fe XI], and [Fe XIV], although this latter feature is strongly blended with [Ca V]. In the infrared region, Lutz et al. (2002) detected [Si IX] $3.94 \mu\text{m}$ (IP = 303 eV). Reunanen, Kotilainen & Prieto (2003) reported long-slit NIR spectroscopy on this object along the direction of the ionisation cone and perpendicular to it. They found strong nuclear coronal lines of

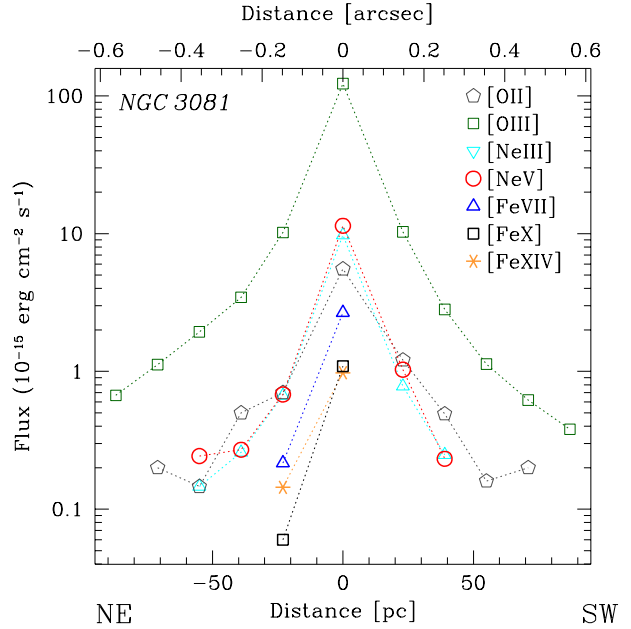


Figure 9. Same as Fig. 1, but for NGC 3081.

[Si VI] $1.964 \mu\text{m}$ and [Si VII] $2.484 \mu\text{m}$, as well as the detection of [Ca VIII] $2.321 \mu\text{m}$ and [Al IX] $2.043 \mu\text{m}$. The coronal [Si VI] line (IP = 166 eV) showed the most extended emission in the $1.5\text{--}2.5 \mu\text{m}$ range studied by these authors, with a flux distribution FWHM of 350 pc and 200 pc parallel and perpendicular to the ionisation cone respectively, suggesting a strongly anisotropic radiation field.

The STIS blue spectra of NGC 3081 show strong, very symmetric, single-peaked lines from low-ionisation (i.e. [O II], [Ne III], and [O III]) and high-ionisation species (i.e. [Ne V], [Fe VII], and [Fe XIV]), as well as permitted hydrogen and helium lines. The most extended CL is [Ne V], which can be traced up to $\sim 40 \text{ pc}$ SW and $\sim 55 \text{ pc}$ NE of the nucleus. It can be seen in Fig. 9 that its flux distribution is nearly symmetrical with respect to the nucleus. The spatial distribution of the lower ionisation gas is also symmetric relative to the maximum of emission located at the unresolved nucleus and compact. [O III] displays the largest emission region, extending up to $\sim 230 \text{ pc}$ SW and NE of the nucleus. The CLs of [Fe VII]H3760 and [Fe XIV] are only detected at the nucleus and next to it towards the NE. No extended emission of these lines is detected to the SW.

The red spectra, of higher spectral resolution, show lines with more complex profiles at both directions from the nucleus. The nuclear spectrum displays a relatively weak, but clearly present, [Fe X] line. However, due to the weakness of this line, little can be said about its detailed profile. As in the case of the other coronal lines, the [Fe X] emitting region is also restricted to the inner region, detected only in the nucleus and at 25 pc NE from it.

It is worth mentioning that the position of the STIS slit is the same as in the observation presented by Reunanen et al. (2003), that is, perpendicular to the cone. However, the coronal emission observed by these authors is much more extended than the one displayed by the optical coronal lines in the STIS data. This can be explained if we consider that the spatial resolution of the Reunanen et al. (2003) data for

NGC 3081 is $1''$ and that the slit width they employed is a factor of ten larger than that of STIS.

3.7 NGC3227, Mrk 348, NGC 5643, and NGC 7682

Although these galaxies exhibit signs of coronal line emission, because of the weakness of these lines or due to the poorer spatial resolution, the analysis of their coronal line emission is restricted to only a few apertures. In Table 3 we report the measurements of the most important lines observed in these galaxies. Below we describe the most important aspects of the HST/STIS spectra of these sources.

3.7.1 NGC 3227

This nearby Seyfert 1 galaxy is classified as a SAB galaxy and is interacting with NGC 3226. It is known for having a compact ($0.4''$) double radio source at PA $\sim 170^\circ$, and [O III] emission extending $\sim 7''$ north-east of the nucleus, in PA $\sim 30^\circ$ (Mundell et al. 1995), meaning that this object may represent another case in which the radio structure and the [O III] are physically misaligned.

Previous reports on high excitation gas in this object are scarce. As in Mrk 3, in spite of the strong cone seen in [O III] images, [Fe VII] in the optical and [Si VI] in the near-infrared (Reunanen et al. 2003; Rodríguez-Ardila et al. 2006) are the lines with the highest ionisation potential reported.

The STIS data were taken along PA= -150° , that is, along the cone axis, where the [O III] emission is preferentially extended, and off the radio jet. The optical spectrum displays weak nuclear emission of [Ne V], [Fe VII], and [Fe X], not detected in any other aperture. At the distance of NGC 3727, this implies that the CLR is restricted to the central ~ 15 pc, making this source the AGN of the sample with the smallest CLR. This result, moreover, puts a tighter constraint on the size of the [Fe VII] gas and agrees with the values reported by Rodríguez-Ardila et al. (2006). Consistently with the optical results here, in the NIR region these authors report that [Si VI] is the only coronal line detected. It is emitted in a very compact zone, observed only up to 45 pc N of the nucleus. To the south, no emission is found. It should be noted that the spectra from Rodríguez-Ardila et al. (2006), both optical and NIR, were taken with the slit aligned along the radio axis. Therefore, it can be concluded that no significant enhancement of the coronal-line gas is observed in this object due to the local interaction between gas and the radio jet.

3.7.2 Mrk 348

Mrk 348 (NGC 262) is classified as a type 2 Seyfert galaxy. Neff & de Bruyn (1983) report that its nuclear radio source consists of a compact core plus two knots aligned along PA= 168° , with a total size of about $0.15''$. They also report variability at 6 and 21 cm on timescales of months. A high-resolution narrow-band HST image published by Capetti et al. (1996) shows a linear structure of narrow-band [O III] $\lambda 5007$ emission extended by $0.45''$ at a position angle of $\sim 155^\circ$.

Detection of optical coronal lines in this objects has

been reported by Malkan (1986) and Cruz-González et al. (1994). They found [Ne V] and [Fe VII], respectively, in the nucleus of this source. Riffel et al. (2006), using NIR spectroscopy, detected conspicuous emission of [S VIII], [Si IX], [Si VI], [Si X], and [Ca VIII].

The HST/STIS data analysed here were taken with the slit at PA= 146° , that is, nearly aligned along the [O III] emission. The only coronal lines observed in these spectra are from Ne $^{+4}$. Lines with ionisation potential higher than 100 eV are not observed. As in the case of the lower ionisation lines (i.e. [O II], [Ne III], and [O III]), the [Ne V] emission is very asymmetric. This line is detected up to ~ 100 pc towards the NW but it is not observed towards the SE beyond the unresolved nucleus. As there is no red spectrum available for this object, nothing can be said about the [Fe X] line.

3.7.3 NGC 5643

This almost face-on barred spiral (Morris et al. 1985) shows a clear dust lane running along the southern leading edge of the bar to the east. Schmitt, Storchi-Bergmann & Baldwin (1994) presented [O III] and H α images, as well as optical spectra of NGC 5643. The images show the [O III] gas to be extended along the east-west direction by $20''$. East of the nucleus the radio jet (PA $\sim 87^\circ$) lies along the southern edge of the ionisation cone (Simpson et al. 1997).

The HST/STIS optical spectrum of NGC 5643 shows [Ne V] and [Fe X] in the nucleus. The latter feature is, however, very weak. [Fe VII] is not detected at the 3σ level in the blue region, while the red spectrum does not include [Fe VII] $\lambda 6086$. However, Morris & Ward (1988) report its detection in the optical spectrum of this source. Overall, the coronal line emission is quite compact and asymmetric. [Ne V], for instance, is found up to 30 pc NE while to the SW it is restricted to the unresolved nucleus. [O III] $\lambda 5007$, in contrast, is significantly more extended to both NE and SW, observed out to nearly 400 pc.

3.7.4 NGC 7682

NGC 7682 is a Seyfert 2 galaxy (Huchra & Burg 1992) in interaction with NGC 7683 (Arp 1966). Ionised gas in H α + [N II] and [O III] is detected on scales of kiloparsecs in this galaxy (Brodie et al. 1987; Durret 1994). In the NIR, only K-band spectroscopy was previously reported by Imanishi & Alonso-Herrero (2004). The only optical coronal line observed in the STIS spectrum of NGC 7682 is [Ne V]. No iron lines or previous reports in the literature of higher ionisation lines in this wavelength interval were found. In the NIR, however, NGC 7682 shows [Si VI] $1.963 \mu\text{m}$ and [S VIII] $0.991 \mu\text{m}$ (Riffel et al. 2007), whose ionisation potential is 167 and 281 eV, respectively. Though weak, the presence of these latter features indicates that, in a photoionisation scenario, high-energy photons reach the NLR.

In addition to the unresolved nuclear [Ne V] emission, this coronal line displays a highly asymmetric extended morphology, observed up to 150 pc NE and 50 pc SW. Due to the low S/N, even for the nuclear spectrum, little can be said regarding the emission line profile. However, nuclear low-ionisation lines are strongly asymmetric, displaying a prominent extended red wing. Beyond the nucleus, the red wing is not observed.

Table 3. Emission line fluxes for Mrk 348, NGC 5643, NGC 3227, and NGC 7682.

Object	Distance [arcsec]	[Ne v] λ3425	[O II] λ3727	[Ne III] λ3869	[O III] λ5007	[Fe VII] λ6086	[Fe X] λ6374
Mrk 348	0.0	4.66(0.32)	18.9(0.34)	10.9(0.33)	148(0.62)	–	–
	0.15 NW	2.14(0.25)	7.61(0.20)	4.47(0.19)	49.5(0.16)	–	–
	0.25 NW	1.81(0.20)	6.96(0.19)	3.69(0.14)	35.2(0.11)	–	–
	0.36 NW	0.74(0.19)	3.38(0.17)	1.33(0.14)	7.45(0.10)	–	–
NGC 3227	0.00	20.00(4.10)	11.90(3.50)	26.70(4.33)	222(2.50)	8.2(2.7)	8.3(3.4)
NGC 5643	0.0	1.14(0.18)	3.49(0.21)	2.10(0.20)	43.3(0.09)	–	2.40(1.10)
	0.15 NE	1.49(0.16)	2.74(0.10)	1.43(0.09)	24.0(0.03)	–	–
	0.25 NE	1.28(0.15)	2.30(0.15)	1.23(0.14)	14.2(0.09)	–	–
	0.36 NE	0.60(0.12)	1.81(0.09)	0.62(0.08)	7.65(0.05)	–	–
NGC 7682	0.0	0.86(0.38)	3.82(0.12)	2.70(0.13)	25.0(0.13)	–	–
	0.15 NE	0.31(0.14)	1.03(0.07)	0.47(0.06)	4.10(0.05)	–	–
	0.25 NE	–	1.04(0.05)	0.45(0.04)	4.57(0.04)	–	–
	0.36 NE	0.26(0.06)	2.27(0.07)	0.79(0.06)	7.78(0.04)	–	–
	0.46 NE	0.25(0.09)	2.11(0.05)	0.70(0.04)	7.13(0.04)	–	–
	0.15 SW	0.17(0.01)	0.92(0.06)	0.23(0.05)	4.43(0.10)	–	–

NOTE – Fluxes are given in units of 10^{-15} erg cm $^{-2}$ s $^{-1}$. In parenthesis we give the corresponding 3σ errors.

Table 4. Observed extent of the coronal lines, in parsecs. [O III]λ5007 is also included for comparison.

	[Ne v] λ3425	[Fe VII] λ3760	[Fe XIV] λ5303	[Fe VII] λ6086	[Fe X] λ6374	[S XII] λ7611	[Fe XI] λ7892	[O III] λ5007
Mrk 3	230 SW	–	–	200 SW	–	–	–	470 SW
	150 NE	–	–	95 NE	–	–	–	710 NE
Mrk 348	< 30 SE	–	–	–	–	–	–	250 SE
	105 NW	–	–	–	–	–	–	610 NW
Mrk 573	150 NW	< 35 NW	85 NW	–	120 NW	–	–	1400 NW
	120 SE	50 SE	50 SE	–	85 SE	–	–	1170 SE
NGC 1068	110 SW	10 SW	–	25 SW	10 SW	10 SW	10 SW	290 SW
	140 NE	130 NE	–	130 NE	115 NE	20 NE	50 NE	375 NE
NGC 3081	40 SW	< 15 SW	< 15 SW	–	< 15 SW	–	–	210 SW
	55 NE	25 NE	25 NE	–	25 NE	–	–	250 NE
NGC 3227	< 10 SW	–	–	< 10 SW	< 10 SW	–	–	50 SW
	< 10 NE	–	–	< 10 NE	< 10 NE	–	–	80 NE
NGC 4151 (221°)	75 SW	–	–	75 SW	10 SW	–	–	450 SW
	70 NE	–	–	30 NE	10 NE	–	–	255 NE
NGC 4151 (70°)	100 SW	–	–	95 SW	10 SW	–	–	210 SW
	75 NE	–	–	70 NE	< 10 NE	–	–	440 NE
NGC 4507	130 NW	130 NW *	35 NW	–	35 NW	–	–	315 NW
	60 SE	60 SE *	35 SE	–	35 SE	–	–	200 SE
NGC 5643	< 10 SW	–	–	–	–	–	–	370 SW
	30 NE	–	–	–	–	–	–	410 NE
NGC 7682	150 NW	–	–	–	–	–	–	560 NW
	50 SE	–	–	–	–	–	–	765 SE

* This was measured from the line [Fe VII]λ3586.

4 KINEMATICS OF THE CORONAL-LINE GAS

The superb spatial resolution of the STIS spectra allows us to study the kinematics of the coronal-line gas at scales down to a few parsecs, and to compare it with that of lower ionisation gas. We are interested, for instance, in studying

if the coronal-line gas is kinematically perturbed and enhanced in regions where the jet interacts with the NLR gas, if it is compatible with disk rotation or if it is associated instead with outflows. To this purpose we constructed radial velocity maps for those objects that display extended CLRs, with more than one line detected at sufficient S/N. In

Figures 10–16 we show the variation of line centroid velocities and FWHMs of the lines as a function of the distance to the nucleus. The velocity curves measured for [O II] and [Ne III] lines are very similar to the ones of [O III], hence we did not include them in the plots. The velocities are given with respect to the systemic velocities of the galaxies derived from their redshifts. Notice that these redshifts, taken from the NASA/IPAC Extragalactic Database (NED), were derived using emission lines, and may have small deviations from the true redshift of the galaxy. In the cases where a line was fitted by two Gaussian components, the velocities of the more blueshifted line is represented by a filled symbol and the other component by an open symbol. If only one component was detected in a line, the velocity is represented by an open symbol. When combining high and low spectral resolution data, the FWHM of the lines derived from the former were not used due to the large difference in the spectral resolutions of both gratings.

In the following subsections we discuss the results obtained for a subset of galaxies of our sample.

4.1 Mrk 573

Fig. 10 shows the variation along the slit of both the FWHM of the most conspicuous lines studied (upper panel) and the radial velocity for the same set of lines (bottom panel) for this object. Note that the FWHMs of [Fe X] were not included in the plot because of the large difference in instrumental resolution between the blue and red spectra. Data for that line, however, was employed to study the radial velocity along the spatial direction of the high-ionisation gas. It can be seen that the radial velocity for [O III] is in perfect agreement with the results presented by Schlesinger et al. (2009, cf. their fig. 4) using the same data for [O III]. The region plotted in Fig. 10 maps the high velocity component of the biconical outflow suggested by these authors. Our results show that [Ne V] and probably [Fe VII], the two coronal lines with the lowest ionisation potential, follow a similar behaviour as [O III], except that the former two are associated with the inner region of the outflow. [Ne V] is seen up to only 150 pc to the NW and 120 pc to the SE. The data for [Fe VII] are less conclusive as only weak [Fe VII] lines in the blue spectra were available. Kinematically, [Ne V] displays a similar rotation curve than [O III] to the SE. In contrast, at ~ 50 pc NW of the centre, both lines appear to diverge: the coronal-line gas is shifted to the blue relative to [O III]. This is consistent with the broadening observed in [Ne V] at this position. At 85 pc NW a spike is observed at the position of the [Ne V] line, and while this line is clearly present, no accurate determination of its shift and FWHM was possible.

This scenario contrasts to what is seen in [Fe X]: It displays a prominent double-peak structure in the region where it is detected². Moreover, the radial velocity implies that it is not part of the biconical outflow, even though spatially, the region emitting [Fe X] coincides with that of [Ne V].

² Kraemer et al. (2009) recently analysed HST spectra of the central emission knot of Mrk 573, extracting a single binned spectrum from the central $1.1''$. They report a higher FWHM of [Fe X] than seen in any other lines, likely due to the line splitting we observe in the spatially resolved data (see also our Fig. 2)

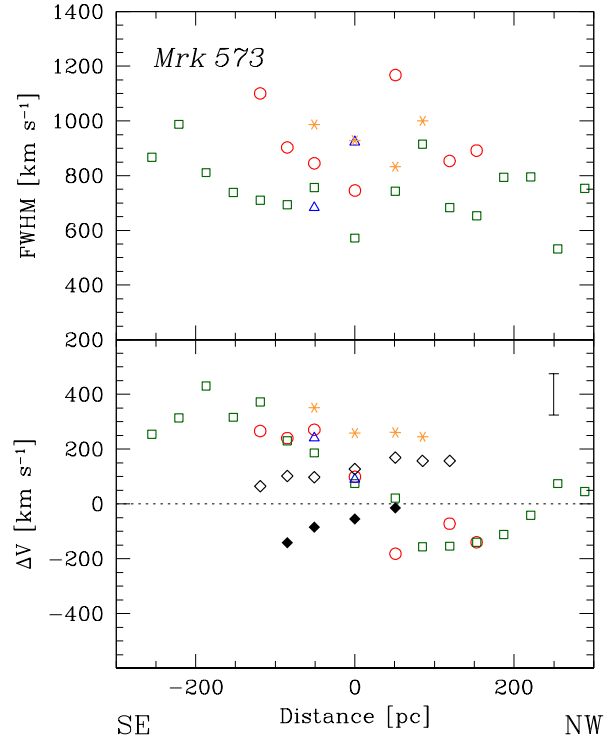


Figure 10. Radial velocity (lower panel) and FWHM (upper panel) of the principal lines measured in Mrk 573 as a function of the projected distance to the nucleus. The filled and open symbols represent a component of a line fitted by two gaussian components. Green squares represent [O III], red circles [Ne V], blue triangles [Fe VII], black diamonds [Fe X], and yellow asterisks [Fe XIV]. The error bar at the upper right corner of the lower panel shows the maximum error of these measurements.

A similar conclusion regarding the rotation pattern can be drawn for [Fe XIV], which shows a completely different behaviour than the lower ionisation lines. At every distance from the nucleus, the [Fe XIV] line is redshifted with respect to the other lines and the systemic velocity of the galaxy. One possible explanation for this unusual behaviour is that [Fe XIV] shows similar, but more extreme, line splitting as [Fe X]. We however, only detect one peak. Another possibility is some contamination in the red wing of [Fe XIV] by [Ca V] $\lambda 5309$.

The FWHM of the coronal lines varies significantly from point to point. For [Ne V], at the unresolved nucleus, we measured a FWHM of 750 km s^{-1} while at 50 pc to the NW it has doubled this value, with a FWHM of 1200 km s^{-1} , broader than any other NLR feature.

4.2 NGC 1068

Many models have been proposed to explain the kinematics of the inner regions of NGC 1068, mainly based on observations of the [O III] $\lambda 5007$ emission line with high-spatial resolution. Axon et al. (1998) suggested that the kinematics of the NLR is governed by the interaction between the NLR gas and the radio outflow observed in this galaxy. Crenshaw & Kraemer (2000), based on the same set of STIS obser-

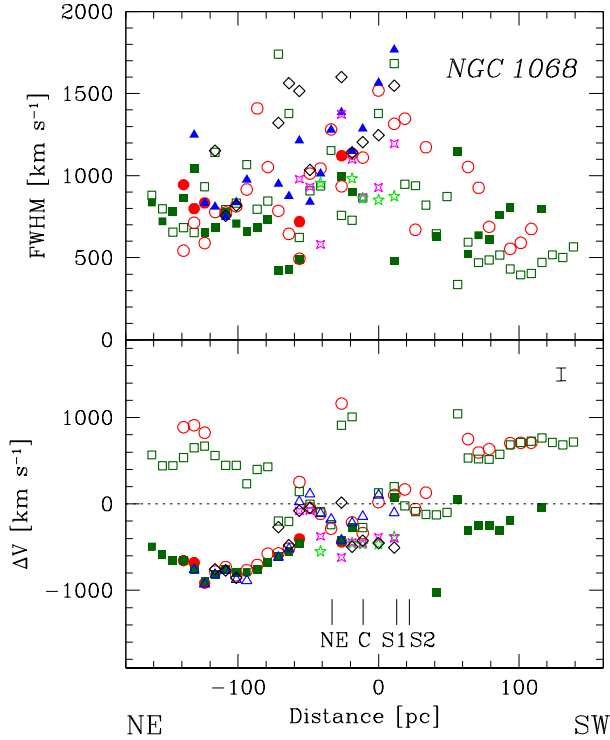


Figure 11. Same as Fig. 10, but for NGC 1068. Here the magenta four-pointed stars represents [Fe XI] and the green five-pointed stars [S XII]. The labels in the lower panel indicate the position of the radio knots intersected by the slit.

vations presented here, concluded that a simple kinematic model of a biconical hollowed outflow gives a reasonable explanation for the velocity field of the [O III] gas. This model assumes a constant acceleration of the clouds in the inner 140 pc and constant deceleration farther out. More recently, Das et al. 2006 re-analysed the radial outflow models and the possible dynamical effects of the radio jet. The models were capable of explaining the large-scale pattern of the [O III] emission. However, lateral expansion due to the radio knots (as proposed by Axon et al. 1998) was required to explain the fainter NLR clouds. They concluded that an interaction between the radio jet and the [O III] emitting gas is possible, but that these interactions are modest.

The STIS slit used to observe NGC 1068 was positioned along the small scale radio jet displayed by this galaxy. In Fig. 11 we show the rotation curve (lower panel) and FWHM (upper panel) of the coronal lines and [O III] measured in NGC 1068 spectra as a function of the distance to the nucleus. The labels indicate the positions where the slit intersects the radio jet knots (see Fig. 2 of Gallimore et al. 1996).

In Fig. 11 we can see the extreme complexity of the velocity field of this galaxy. While the [O III] line is double peaked in the inner 140 pc, with one component redshifted and another blueshifted, the [Fe VII] and [Ne V] lines are mostly single peaked, following the redshifted [O III] component towards the SW of the nucleus and the blueshifted [O III] component towards the NE. Exceptions to this are the more external [Ne V] emission regions (from 125 pc to

140 pc NE) where the lines show a second component redshifted by about 1000 km s^{-1} , almost coincident with the redshifted component of [O III], and a high velocity cloud ($\Delta V = 1200 \text{ km s}^{-1}$) located near the nucleus at 25 pc NE. Despite these differences, the overall behaviour of [O III], [Fe VII], and [Ne V] is rather similar, showing a nice symmetric pattern. Moreover, the [Fe X] line also seems to follow the blueshifted component of the [O III] line at the NE side of the nucleus. At the nucleus and 10 pc SW the [Fe X] is blueshifted with respect to the lower ionisation emission lines, with $\Delta V \sim 500 \text{ km s}^{-1}$. On the other hand, the higher ionisation [Fe XI] and [S XII] lines are slightly blueshifted with respect to lower ionisation emission lines, and seem to share the same overall kinematics. This blueshift is about 500 km s^{-1} with respect to the systemic velocity of the galaxy, except for the [Fe XI] line emitted at 40 pc and 50 pc NE which has almost the same velocity as the galaxy, as is the case for the [Fe X] and [Fe VII] lines.

In the upper panel of Fig. 11 we show the variation of FWHM with the distance from the nucleus. These values cover a wide range of velocities, from about 300 km s^{-1} to $\sim 1800 \text{ km s}^{-1}$. No clear correlation between the FWHM and IP of the lines is observed.

We can see in Fig. 11 a strong similarity between the velocity curves of the CLs and [O III], suggesting a common origin. Moreover, the velocity curves and FWHMs of the lines are not especially perturbed at the positions of the radio knots. This implies that the radio jet does not have a significant local influence over the coronal and [O III] emission-line gas kinematics.

4.3 Mrk 3

The STIS slit used in the observations of Mrk 3 coincides with the position of the radio jet reported by Kukula et al. (1993). Therefore, it is another excellent opportunity to study the small scale relation between the radio and the coronal line emission and its influence on the kinematics of the gas. In Fig. 12 we present the radial velocities (lower panel) and FWHMs (upper panel) of the principal lines detected in this galaxy as a function of the distance to the nucleus. The labels in the lower panel indicate the position of the radio features intersected by the slit (see Fig. 2 of Kukula et al. 1999).

In the lower panel of Fig. 12 we can see that the inner regions of Mrk 3 display line profiles splitted into two distinct velocity systems, one redshifted and the other blueshifted with respect to the systemic velocity of the galaxy. Outwards (more than 120 pc SW and 100 pc NE) only the redshifted component is observed. There is a general trend of the line-emitting gas to accelerate as one moves away from the nucleus, it reaches a maximum velocity at about 100 pc from the centre, and then decelerates back to the systemic velocity of the galaxy 100 pc farther out. The maximum redshift of the [Ne V] and [Fe VII] lines, $\Delta V \simeq 550 \text{ km s}^{-1}$, is achieved at 70 pc SW and 90 pc SW, respectively. The maximum blueshift of these lines is reached at 65 pc NE from the nucleus and is slightly higher than the redshift ($\Delta V \simeq 750 \text{ km s}^{-1}$). As in the case of NGC 1068, the velocity structure and FWHM of the lines do not seem to be correlated with the positions of the radio jet knots. However, the line splitting is observed almost all along the fraction of

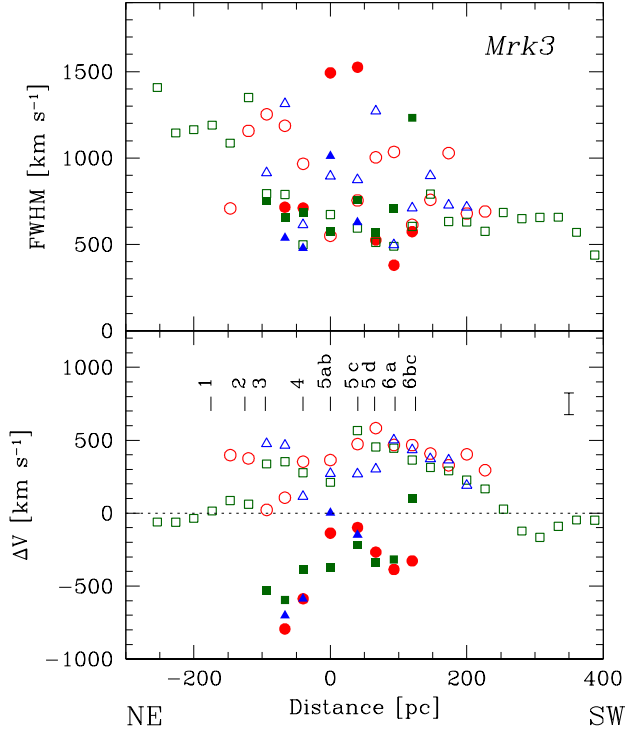


Figure 12. Same as Fig. 10, but for Mrk 3. The labels indicate the position of the radio knots intersected by the slit.

the jet probed by the slit. Moreover, no trend is observed in the FWHMs of the lines, which strongly vary with the distance from the nucleus, from $\sim 400 \text{ km s}^{-1}$ up to the extreme value of the $[\text{Ne V}] \lambda 3425$ line of $\text{FWHM} \sim 1500 \text{ km s}^{-1}$ in the nucleus and 40 pc to the SW.

Previous kinematic models for the $[\text{O III}] \lambda 5007$ emitting gas of Mrk 3 were analysed by Ruiz et al. (2001) based on the same set of data used in this work together with $[\text{O III}]$ slitless spectra. The best fit model indicates that the NLR gas is located in a partially filled bicone and is accelerated radially away from the nucleus and then decelerates at a constant rate. Another kinematic model was proposed by Cappeti et al. (1999), in which the gas forms part of an expanding cocoon of gas circumscribing the radio jet.

The similar behaviour presented by the CLs and $[\text{O III}]$ suggests that the $[\text{Ne V}]$ and $[\text{Fe VII}]$ gas is also part of the same outflow that governs the lower ionisation gas in the central 400 pc of Mrk 3. However, some deviations from the $[\text{O III}]$ emission-line gas are present, mainly towards the NE. At a distance of 70 pc and 90 pc NE from the nucleus, the $[\text{Ne V}]$ lines are blueshifted with respect to the $[\text{O III}]$ lines by an amount of $\Delta V \sim 400 \text{ km s}^{-1}$, whereas further out the trend reverses and the $[\text{Ne V}]$ lines are redshifted with respect to the lower ionisation lines.

4.4 NGC 4151

High-resolution spectroscopy based on HST data has been employed by several authors to study NGC 4151. The kinematics derived from HST long slit observations of $[\text{O III}]$

(Nelson et al. 2000; Crenshaw et al. 2000) show evidence of three components: a low velocity system, consistent with normal disk rotation, a high velocity system in radial outflow at a few hundred km s^{-1} , and an additional high velocity system with velocities up to 1400 km s^{-1} , as previously found from STIS slitless spectroscopy (Hutchings et al. 1998, 1999; Kaiser et al. 1999). The general consensus points to signatures of a radial outflow in the form of a wind, with no interaction with the radio jet.

Overall, the rotation curves found for $[\text{O III}]$, shown in the lower panel of Fig. 13 and Fig. 14, are consistent with that derived by Crenshaw et al. 2000. Along $\text{PA}=221^\circ$, a velocity gradient of over 500 km s^{-1} in the inner 50 pc NE of the nucleus is detected, with all lines being redshifted. The gas first accelerates to a maximum velocity of 500 km s^{-1} relative to the systemic velocity of the galaxy. It then decelerates back to about 100 km s^{-1} at ~ 100 pc. Towards the SW, at ~ 30 pc from the centre, a double-peak structure is detected, with the red peak accompanying the systemic velocity of the galaxy and the blue peak shifted by $\sim 700 \text{ km s}^{-1}$ to the blue from the former. The relative separation between both peaks decreases in the next few parsecs outwards. At ~ 45 pc from the centre, only the red peak is detected. From that point, it suffers a slight acceleration to the blue, reaching 250 km s^{-1} at 70 pc, and then decelerates to 200 km s^{-1} at 100 pc. Along $\text{PA}=70^\circ$ the velocity curve is more flat, deviating very little from the systemic velocity of the galaxy. At ~ 25 pc SW the lines reach a maximum blueshift of $\sim 400 \text{ km s}^{-1}$. Further out, at about 65 pc SW, a second peak in the $[\text{O III}]$ lines is measured, with a blueshift of $\sim 1000 \text{ km s}^{-1}$, not seen in the CLs. This splitting of the lines coincides with the component C2 of the radio jet. The highest ionisation line detected in NGC 4151 is $[\text{Fe X}] \lambda 6374$. When detected, this line has the same velocity as the lower ionisation gas mapped by $[\text{O III}]$, $[\text{Ne V}]$, and $[\text{Fe VII}]$. In the lower panel of Fig. 14 we marked the positions where the slit intersects the radio knots. From this, it is clear that there is no correlation between the radio emission and the CL kinematics, suggesting that the radio jet has no significant influence on the overall kinematics of the gas emitting the CLs.

The variation of FWHM with the distance from the nucleus is plotted in the upper panel of Fig. 13 and Fig. 14. It is easy to see that there is a large scatter in FWHM from point to point, both for lines of the same element and among lines of different species. Overall, the scatter in FWHM among the different ions is the largest in the region where double-peaked lines were detected. This may imply that a number of lines are actually double-peaked, but no longer spectroscopically resolved.

Our radial velocity curves derived from the STIS data which includes, for the first time, the coronal lines $[\text{Ne V}]$, $[\text{Fe VII}]$, and $[\text{Fe X}]$ (see Fig. 13 and Fig. 14) show that these CLs follow the kinematics traced by $[\text{O III}]$. This implies that they follow the same velocity field and originate from the outflow itself, with no important influence of the radio jet.

4.5 NGC 4507

Fig. 15 shows the radial velocity field (lower panel) and FWHM (upper panel) of the principal lines measured for NGC 4507 along the slit. The velocity curve of this galaxy

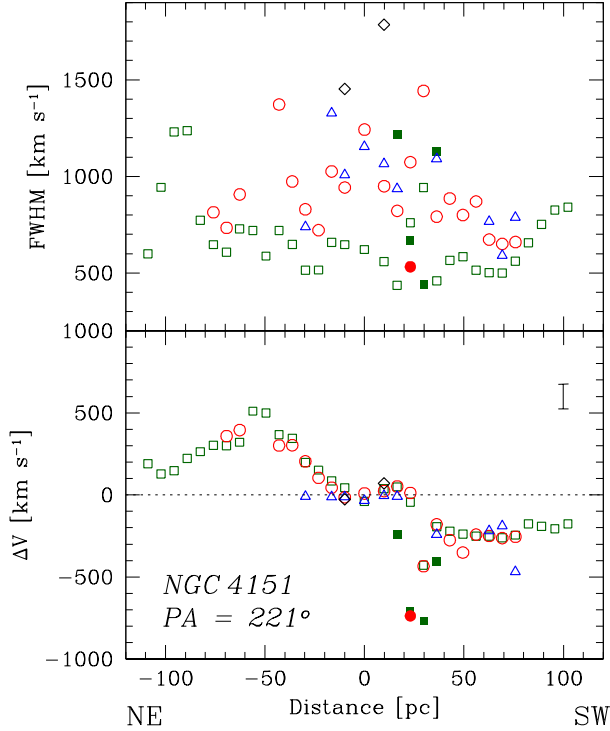


Figure 13. Same as Fig. 10, but for NGC 4151 at PA = 221°.

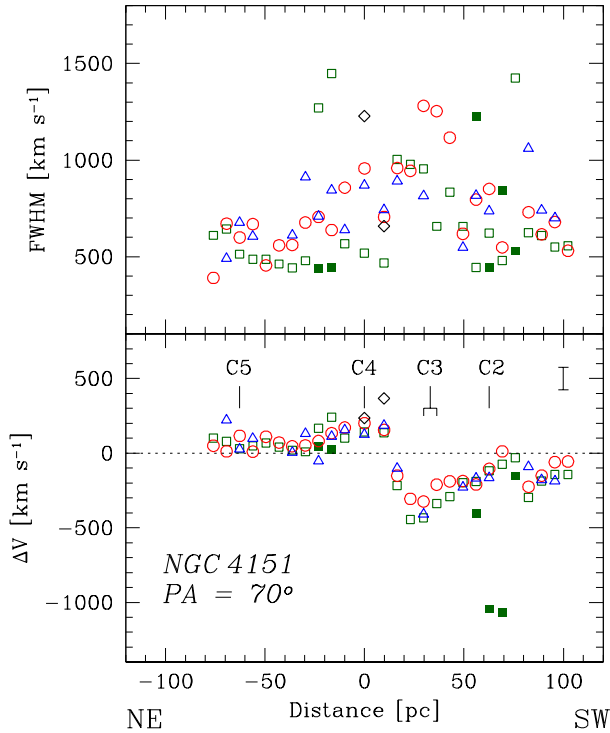


Figure 14. Same as Fig. 10, but for NGC 4151 at PA = 70°. The labels in the lower panel indicate the position of the radio knots intersected by the slit.

is very different to the ones studied in the previous sections, showing a rather flat pattern with velocity shifts closer to the systemic velocity of the galaxy. At the nucleus, the [O III] line displays a double-peaked profile, with one component redshifted by $\Delta V = 200 \text{ km s}^{-1}$ and another blueshifted by $\Delta V = 550 \text{ km s}^{-1}$. At this point the coronal lines of [Ne v] and [Fe VII] show a small blue asymmetry, but the two components are not resolved. The centre of these lines coincides with the red component of [O III]. The maximum of this asymmetry is reached at $\sim 35 \text{ pc}$ NW, where the strongest lines (i.e. [O III] and [Ne v]) can be characterised by the sum of two gaussians separated by $\Delta V \sim 600 \text{ km s}^{-1}$. One component describes a strong narrow core (FWHM $\sim 500 \text{ km s}^{-1}$) and the second component represents a blueshifted wider (FWHM $\sim 1500 \text{ km s}^{-1}$) part. Notice that the [Fe VII] velocity at this point coincides with the ones of the blueshifted components of [O III] and [Ne v]. The blue asymmetry smoothly vanishes as one moves away from the nucleus and a tenuous red wing appears in the emission lines emitted in the outer regions. Further out, where no coronal lines are observed, the [O III] lines in the NW side of the nucleus are double peaked, showing a strong blueshift that reaches 750 km s^{-1} . In general, we can see that the [Ne v] and [Fe VII] emitting gas share the same kinematics with the [O III] gas, with a weak tendency of the [Fe VII] lines to be redshifted with respect to the other two lines. On the other hand, the [Fe XIV] line is redshifted with respect to the lower ionisation lines, with a maximum shift of 500 km s^{-1} at the nucleus. As we mentioned in Section 4.1, the possible presence of weak [Ca v] 45309 on the [Fe XIV] red wing can be, in part, the reason for the measured shift.

The higher resolution red spectra show lines with much more complex structures. As this spectrum was taken with the slit positioned in a different angle than the blue spectrum, we do not include the [Fe X] line in Fig. 15. As we mentioned in Section 3.5, two components were required to describe the nuclear [Fe X] line: one low velocity, broad component ($\Delta V = 155 \text{ km s}^{-1}$, FWHM = 685 km s^{-1}) and a narrow component (FWHM = 130 km s^{-1}) redshifted by 350 km s^{-1} with respect to the systemic velocity of the galaxy. These components are consistent with the velocity-shifts and FWHMs measured for the higher velocity [O I] lines, the latter being slightly broader than the former. No counterpart for the more intense [O I] component was detected in [Fe X]. At both sides of the nucleus, the [Fe X] line profiles were described by one gaussian component with velocities redshifted by 250 km s^{-1} and FWHM = 550 km s^{-1} .

4.6 NGC 3081

Very little information exists in the literature on the kinematics of the spatially resolved NLR gas of NGC 3081 (Ruiz et al. 2005). Here, we used the STIS spectra to map the kinematics of the [O III], [Ne v], [Fe VII], [Fe X], and [Fe XIV] emission-line gas in the inner 200 pc of this galaxy.

As in the case of NGC 4507, the rotation curve of NGC 3081 (lower panel of Fig. 16) is fairly flat. The velocity of the [O III] emitting gas is no greater than a few kilometres per second, with a maximum of $\sim 150 \text{ km s}^{-1}$ at the nucleus. The FWHMs of the [O III] line are very similar, with little variation along the spatial direction. The velocity dispersion of the coronal emission lines is slightly higher, with

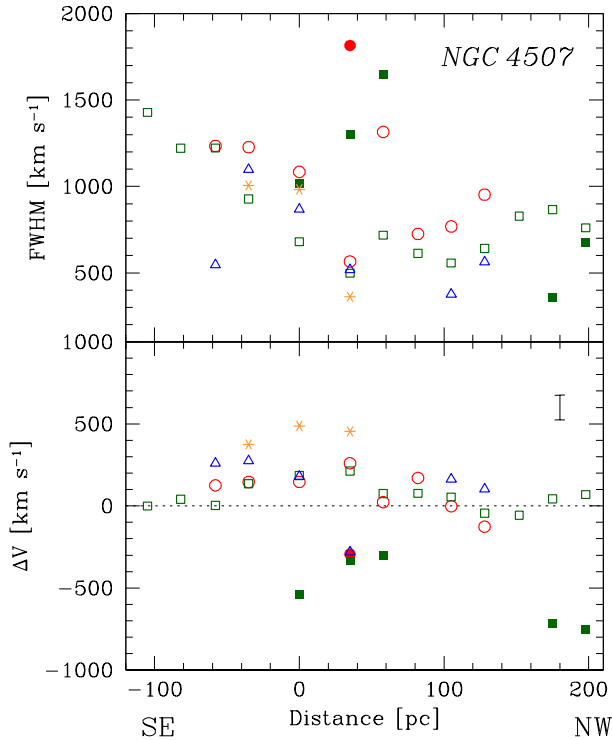


Figure 15. Same as Fig. 10, but for NGC 4507.

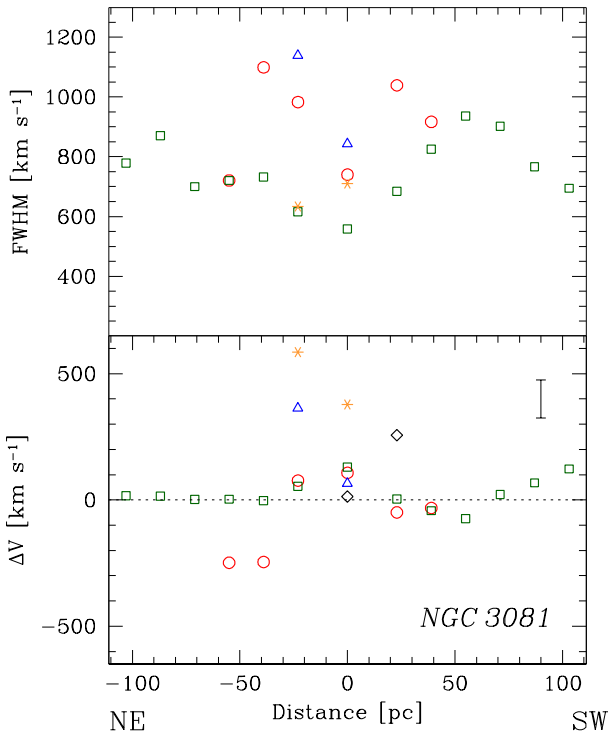


Figure 16. Same as Fig. 10, but for NGC 3081.

the lines either blueshifted or redshifted with respect to the systemic velocity of the galaxy. At the nucleus, all lines but [Fe XIV] have the same shift of the line peak, corresponding to the systemic velocity of the galaxy. At this point, the [Fe XIV] line shows a receding velocity of $\sim 400 \text{ km s}^{-1}$. Next to the nucleus ($\sim 25 \text{ pc NE}$ and SW), the gas producing lines with $\text{IP} > 100 \text{ eV}$ is redshifted by more than $\Delta V = 250 \text{ km s}^{-1}$. The maximum velocity is achieved by the [Fe XIV] emitting gas, which presents a $\Delta V = 600 \text{ km s}^{-1}$. Further out, at ~ 45 and 55 pc NE , the [Ne V] lines are blueshifted by $\Delta V = 250 \text{ km s}^{-1}$.

If we take into account that NGC 3081 is a galaxy observed nearly face-on, gas in a rotating disk aligned with the equatorial plane of the galaxy will be observed with the same systemic velocity of the galaxy. This seems to be the case of the [O III] emission-line gas. On the other hand, the higher dispersion of velocity and FWHM shown by the coronal-line gas suggest that it is governed by different kinematics than the [O III] emitting gas. The CLR of this AGN is rather turbulent and chaotic. Moreover, no coincidence in the FWHM or peak velocity between coronal lines of similar ionisation potential is found, indicating that they are produced in different regions along the line of sight.

5 DEMYSTIFYING THE CORONAL-LINE REGION OF ACTIVE GALACTIC NUCLEI

The high-spatial resolution achieved with STIS allowed us to study not only the global characteristics of the optical coronal line emitting gas but also, for the first time, its small scale properties as a function of the distance to the active nucleus. In this section we discuss the general results that are obtained from the analysis of these data, including the location of the coronal line emitting region, the origin of this emission, and its relation with the radio jets.

5.1 Summary of key results

The spectra analysed in this work revealed multi-component and very complex CLRs, showing a clumpy morphology similar to the one displayed by the low-ionisation lines. The most extended CLs, [Ne V] and [Fe VII], are observed from a few parsecs up to hundreds of parsecs from the nucleus. The *most compact* CLR is observed in NGC 3227, where the [Ne V] and [Fe VII] extent is restricted to the central $\sim 15 \text{ pc}$. On the other hand, Mrk 3 exhibits the *largest* [Ne V] and [Fe VII] emission regions, with a total extent of 375 pc and 300 pc , respectively. The higher ionisation lines (with $\text{IP} > 100 \text{ eV}$), [Fe X], [Fe XI], [Fe XIV], and [S XII], are emitted in more compact regions. [Fe X] is the most extended of this group of lines, varying from 15 pc up to 200 pc , while the other lines are always observed much closer to the nucleus, in regions of less than 100 pc diameter. Broadly speaking, a stratification is observed, in the sense that lines with higher ionisation potentials are more concentrated towards the centre. One interesting aspect is that some objects show a lack of coronal lines with IP larger than 100 eV even though they display strong and extended soft X-ray emission.

From the analysis of the kinematics of the emission-line gas, we found that the CLs tend to follow the same velocity distribution as [O III], in particular the [Ne V] and

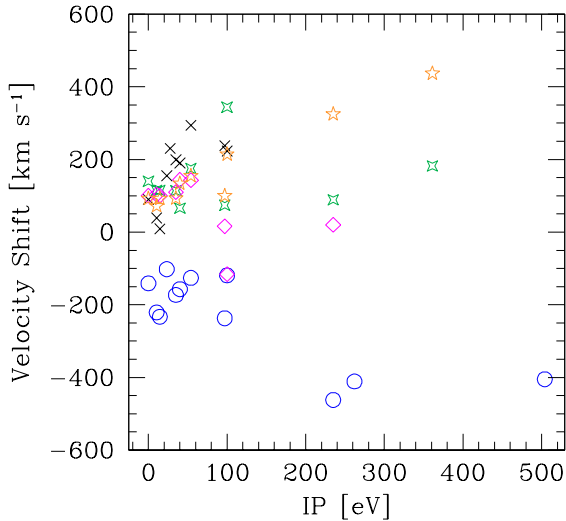


Figure 17. Velocity shift of the lines measured in the integrated spectra of the galaxies as a function of the IP. The black crosses correspond to the lines measured in Mrk 3, green four-point stars to Mrk 573, blue circles to NGC 1068, magenta diamonds to NGC 3081, and yellow five-point stars to NGC 4507.

[Fe VII] lines. Line splitting is sometimes observed in coronal and lower ionisation lines (e.g. [Ne V], [Fe VII], [Fe X], and [O III]). In those cases where [Fe XIV] was observed, the line centre was redshifted with respect to the lower ionisation lines. This means that no universal trend between line shift and IP is observed when high-spatial resolution is employed. This is in contrast with previous reports from low-spatial resolution spectroscopy, usually integrating the *whole* NLR, where the peak of the CLs tend to be more blueshifted than lower ionisation lines (e.g., De Robertis & Osterbrock 1984; Appenzeller & Östreich 1988; De Robertis & Shaw 1990; Marconi et al. 1996; Reunanen et al. 2003). In order to check if the same trend is also apparent in our particular galaxies, we integrated the light distribution along the slit mimicking a seeing-limited observation. We then measured the shift of the central peak of the lines and plotted them as a function of IP as shown in Fig. 17. It can be seen that in Mrk 573 and NGC 3081 no correlation is present at all, while in NGC 4507 the shift of the lines increases with the IP. The trend shown by the latter was previously reported by Appenzeller & Östreich (1988). Only in NGC 1068 a tendency for high-ionisation lines to be more blueshifted than lower ionisation ones can be confirmed.

Three of the galaxies in the sample (NGC 4151, NGC 1068, and Mrk 3) were observed with the slit along the nuclear radio jets they exhibit. From the comparison of the radio and line emission we generally found no enhancement of the coronal line emission, or perturbations of its kinematics, at the positions of the radio knots.

5.2 Origin of the coronal line emission

Two key types of models might explain the coronal lines and their properties: either photoionisation by the central

continuum source (e.g., Korista & Ferland 1989; Oliva et al. 1994; Ferguson et al. 1997a; Binette et al. 1997; Nagao et al. 2003; Mullaney et al. 2009), or shock ionisation or other processes directly or indirectly linked to the presence of radio jets (e.g., Tadhunter et al. 1988; Viegas-Aldrovandi & Contini 1989; Morse, Raymond & Wilson 1996; Axon et al. 1998).

We discuss these possibilities in turn. In the context of photoionisation, important parameters which would affect the measured coronal line spectrum are the shape and strength of the ionising continuum [either from a central “point source” and/or including spatially extended emission as it has been observed in several nearby Seyfert galaxies (e.g., NGC 1068: Young et al. 2001; NGC 4151: Ogle et al. 2000)], the gas density, the cloud column densities (matter-bounded versus ionisation-bounded), and the metal abundances, which however, should have no strong local variations.

The presence of radio jets could affect the emission-line ratios and kinematics in several major ways: firstly, by collisional ionisation from local shocks directly originating from jet-cloud interactions. In this scenario gas is heated up to temperatures of several 10^6 K and a close spatial coincidence between jets and gas clouds is expected. Secondly, shocks can compress the gas which in turn is photoionised by the central source (Viegas-Aldrovandi & Contini 1989). In this case a close link between the jet and the morphology and kinematics of the emission-line gas is expected. Thirdly, jet-cloud interactions could lead to fast auto-ionising shocks (Dopita & Sutherland 1995, 1996), photoionising surrounding gas. A grid of models taking into account ionisation by the central source, the diffuse radiation of shocked and ionised gas, and collisional ionisation were presented by Contini & Viegas (2001). The application of these models to AGNs shows that indeed, fast shocks could be responsible for a fraction of the observed line flux. Finally, jet-gas interaction might produce cocoons and lateral flows, affecting gas at larger distances than directly at the loci of the jet axis (Taylor, Dyson & Axon 1992; Steffen et al. 1997).

The physics of jets and their interaction with the surrounding medium is highly complex. Moreover, this scenario is even more complicated when we also consider the additional effect of ionising photons from the central continuum source. Jets might have indirect effects on the local gas physics, even if photoionisation is the dominant ionisation source; e.g. by locally enhancing the gas density. Such a case is difficult to rule out, since the presence of the jet would mostly add to the spectral complexity of the line emission, without directly accounting for all its features.

5.2.1 Coronal lines and their relationship with radio jets

The tendency of photoionisation models to underpredict the highest-ionisation CLs, and the spatial coincidence between the radio and high-ionisation emission, led several authors to suggest that fast shocks driven by radio jets can play an important role in the formation of CLs (e.g., Axon et al. 1998). In order to address this point we selected from the initial sample of objects three galaxies, Mrk 3, NGC 1068, and NGC 4151, which show a strong, highly collimated small-scale radio jet. The HST/STIS data of these galaxies are particularly suitable to test the hypothesis of shocks as pre-

cursors of the CLs since the slits used in the observations were nearly aligned with the radio jets.

In Sections 3.2, 3.3, and 3.4 we described the main properties of NGC 1068, Mrk 3, and NGC 4151, and the results obtained from the measurements of their coronal-line fluxes. We showed that, in spite of the similarities in the radio emission displayed by these galaxies, there is a notable difference between them: while NGC 1068 displays CLs with a wide range of ionisation potentials, from 99 eV up to 505 eV, NGC 4151 only shows coronal lines of IP < 300 eV. The case of Mrk 3 is even more critical as the only coronal lines detected are those of IP \sim 100 eV. Moreover, the intensity distribution of these lines shows a similar morphology than the lower ionisation lines of [O III] and [Ne III]. Furthermore, there is no enhanced emission at the positions where the radio knots are observed. In particular, NGC 4151 was observed at two position angles, one along the radio jet and the other 30 deg away from the radio axis. The line intensities and line ratios are remarkably similar at these two positions, not showing any signs of increased emission along the position of the radio jet, as noticed by Nelson et al. (2000). Additionally, the kinematics of the CLs (Section 4.2 for NGC 1068, Section 4.3 for Mrk 3, and Section 4.4 for NGC 4151) do not seem to be locally affected by the radio jet. In none of the three cases we see a correlation between the position of the radio knots and the velocity field or the FWHM of the lines. Although several models have been proposed to explain the velocity curves of these galaxies, including models involving jet-cloud interaction, the simple model of a radial outflow (Nelson et al. 2000; Crenshaw & Kraemer 2000; Ruiz et al. 2001; Crenshaw et al. 2000) was able to successfully reproduce the kinematics of [O III] for the three galaxies and, therefore, also the kinematics of the CLs.

Additional information about the jet-CL interaction is provided by the galaxy Mrk 573. This galaxy also harbours a strong radio jet in its nucleus, but unfortunately the STIS slit was positioned in another direction and does not intersect the radio knots. However, it can still give us useful information. Mrk 573 represents an extreme case of [Fe X] emission. The coronal line emission is strongly peaked, with the maximum in the nucleus and no relation at all with the knots and arcs seen in the WFPC2 F606W filter image by Pogge & Martini (2002). This scenario is reinforced by Whittle et al. (2005) and Schlesinger et al. (2009), who presented detailed calculations of the radio jet energetics and its modest impact on the gas ionisation. They both showed, for Mrk 78 and Mrk 573 respectively, that the central source is the main driver for the observed luminosity, while the mechanical luminosity associated to the outflow accounts only for a few percent of the estimated bolometric luminosity.

As we mentioned above, in some cases, shocks can lead to very high temperatures in the line-emitting gas. In order to check the temperatures, we employed the standard diagnostic [O III] (4958+5006)/4363 line ratio to determinate the temperature of the O⁺² gas as a function of the distance to the nucleus (Fig. 18). We found temperatures ranging from \sim 10000 – 20000 K at most for the positions where the ratio could be determined. The temperatures derived for the inner regions of NGC 4151 are probably overestimated due to a strong blend of the [O III]4363 line with the broad line of H γ . Temperatures lower than 20000 K are typical of photoionised gas, and do not indicate any additional en-

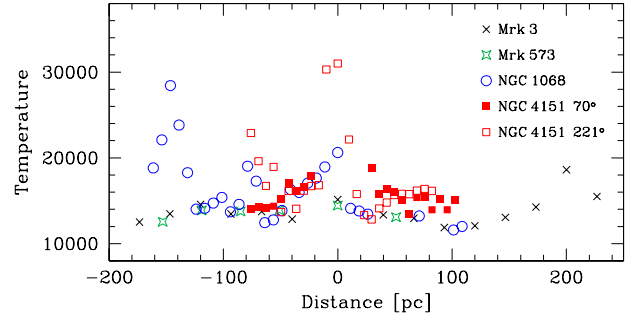


Figure 18. Gas temperature measured from the [O III] lines for Mrk 3, Mrk 573, NGC 1068, and NGC 4151.

ergy input source, as would be the case of shocks strongly interacting with the gas. Although these temperatures were measured for the [O III] region, the similarity between the CLs and lower ionisation gas suggests a common origin and therefore no important contribution of shocks to the CLs.

From all the above, we see that there is no clear evidence of a *local* influence of the radio jet on the coronal-line gas. However, there is the possibility of the presence of hot cocoons generated by the radio jet that affect the gas located at larger distances from it. In this scenario, the velocity curves are expected to form a broken ellipsoid, with the approaching gas strongly blueshifted and the receding gas strongly redshifted, independent of the observation angle. We can discard the presence of an expanding cocoon in the case of NGC 4151, since the lines displayed by this galaxy have only one component. For NGC 1068 and Mrk 3 this scenario can not be tested with the data presented here. However, integrated emission-line fluxes from long slit spectroscopy (Koski 1978) show that, in the case of Mrk 3, the ratio of [Fe VII]/[O III] is very similar to that measured from the STIS data, implying that if cocoons have any impact on the coronal line emission it should be quite small.

Although we can not completely discard the contributions of shocks to the formation of the CLs, the lack of correlation between the positions of the radio knots and the flux distribution and kinematics of the CLs in these galaxies, and the different ionisation ranges displayed by them, suggest that the interaction of the radio jet with the surrounding gas does not have a major effect in the emission of the CLs locally. However, with the data presented here, we can not exclude the presence of expanding cocoons formed by the radio jet in NGC 1068 and Mrk 3. Further progress can be achieved from the analysis of 3D spectroscopy, mapping the emission-line gas not only along the radio jet but also the gas located a larger distances from it.

5.2.2 Predictions from photoionisation modelling

In this Section, we compare the observed emission-line ratios with photoionisation models. In a first step, we compare model predictions for the low-ionisation line ratio [O II]/[O III] versus that of [Ne III]/[Ne V]. In a second step, we focus on the higher ionisation CLs, for which fewer model predictions are available.

Two model approaches have been followed in the past. On the one hand, authors have attempted to match CL

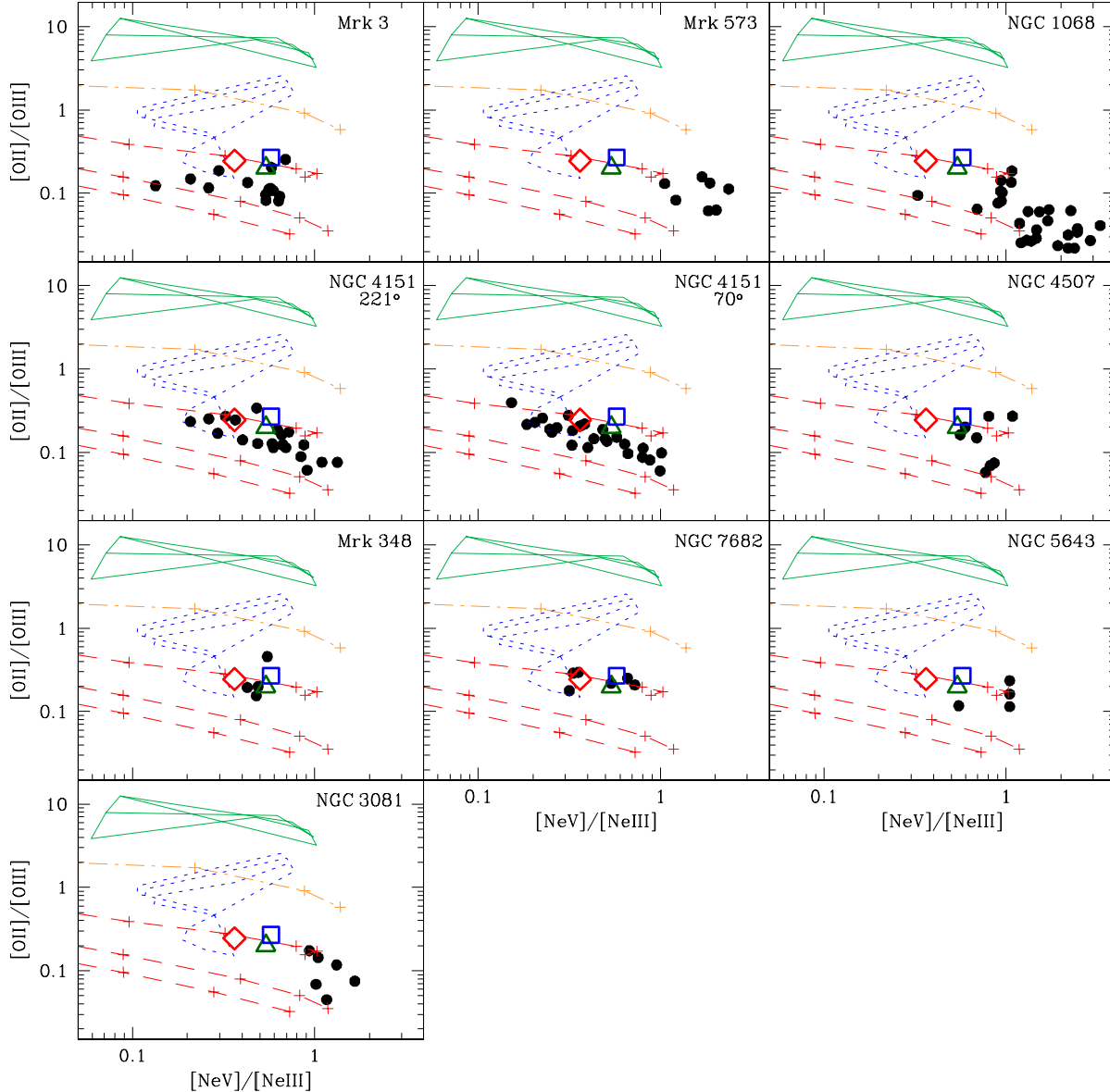


Figure 19. $[\text{OII}]/[\text{OIII}]$ versus $[\text{NeV}]/[\text{NeIII}]$ line ratios diagram. The points correspond to the line ratios measured in the galaxies of the sample at different distances from the nucleus. Red pluses linked by dashed-lines correspond to the predictions of optically-thick single-slab power-law photoionisation models with spectral indices of -1.0 , -1.5 , and -2.0 (from top to bottom), and a sequence in the ionisation parameter covering the range $5 \times 10^{-4} < U < 10^{-1}$, increasing from left to right (see fig. 4 of Tadhunter 2002). Orange pluses linked by a dot-dashed line correspond to the predictions of photoionisation models including matter-bounded clouds of Binette, Wilson & Storchi-Bergmann (1996), with the $A_{\text{M}/\text{I}}$ parameter covering the range $10^{-4} < A_{\text{M}/\text{I}} < 1$, increasing from left to right. Green solid lines and blue dotted lines correspond to pure shocks and “50% shock + 50% precursor” models from Dopita & Sutherland (1996), respectively. Each sequence corresponds to a fixed magnetic parameter ($B/\sqrt{n} = 0, 1, 2, 4 \mu\text{G cm}^{-3/2}$) and a shock velocity v_s varying between 150 and 500 km s^{-1} . The green triangle corresponds to Ferguson et al. (1997a) models. The blue square and red diamond represent the BB20 and PB50 models of Komossa & Schulz (1997), respectively.

strengths in *samples* of Seyfert galaxies, with an eye on the highest observed line ratios of CLs relative to low-ionisation lines (e.g., Erkens et al. 1997; Komossa & Schulz 1997; Binette 1998; Rodríguez-Ardila et al. 2002; Nagao et al. 2003; Rodríguez-Ardila et al. 2006). On the other hand, attention has focused on individual well-studied Seyfert galaxies which have spatially resolved NLRs, and photoionisation models have been presented which successfully reproduce the emis-

sion line ratios (with focus on low-ionisation lines, but including $[\text{NeV}]$ and $[\text{FeVII}]$) of individual clouds. For the STIS spectra analysed here, this was done for NGC 4151 (Nelson et al. 2000; Kraemer et al. 2000), Mrk 3 (Collins et al. 2005, 2009), and NGC 1068 (Kraemer & Crenshaw 2000a). These photoionisation models assume two or three different components of ionised gas (at each distance from the nucleus), photoionised directly by a power-law continuum and by an

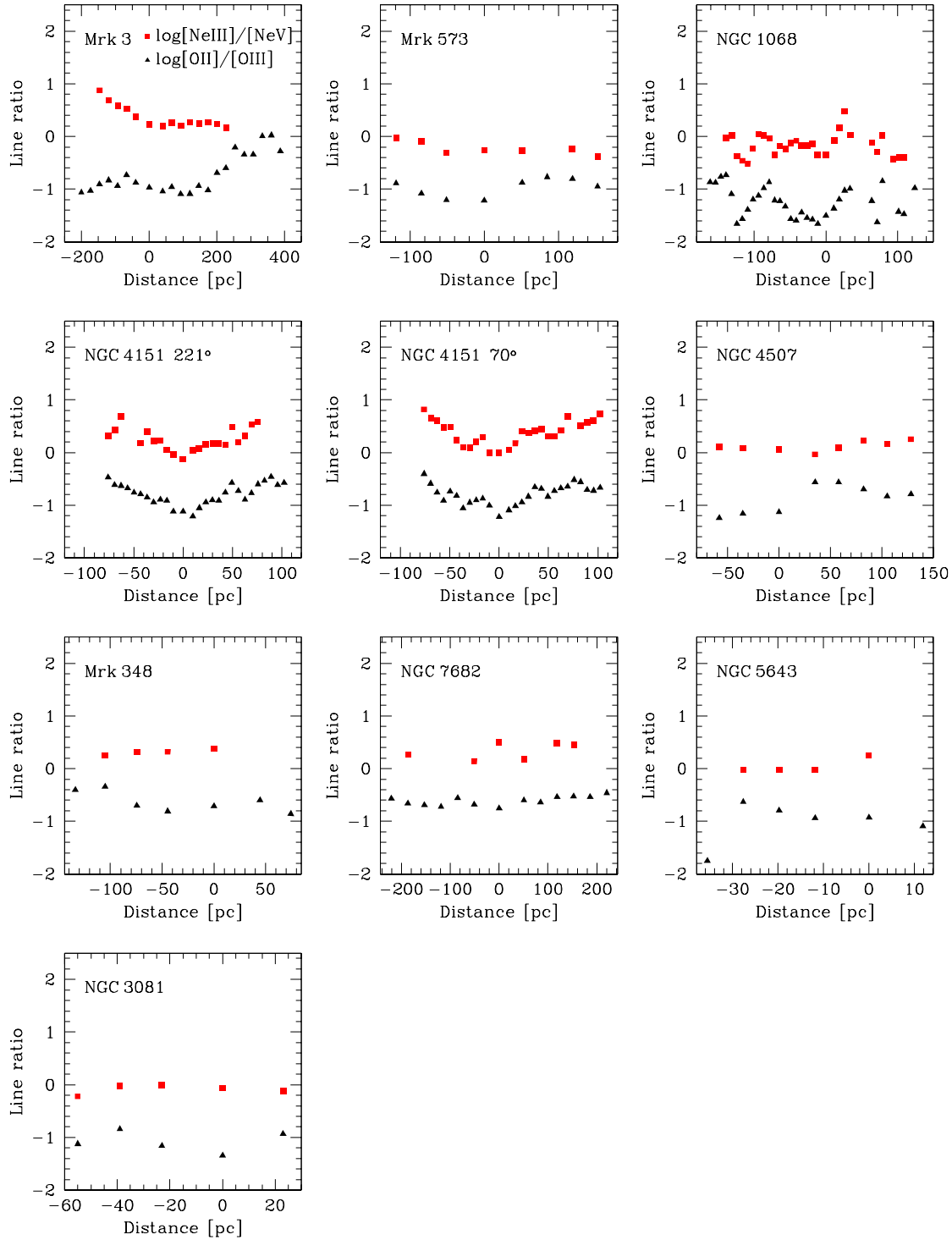


Figure 20. $[\text{O II}]/[\text{O III}]$ (black triangles) and $[\text{Ne III}]/[\text{Ne V}]$ (red squares) line ratios as a function of the distance to the nucleus of the galaxies in the sample.

absorbed continuum in the case of the low-ionisation component. Similar models were used to reproduce high- and low-ionisation lines detected in the nuclei of Mrk 573 (Kraemer et al. 2009) and NGC 1068 (Kraemer & Crenshaw 2000b).

A selection of different models, including photoionisa-

tion models with a mix of matter- and ionisation-bounded clouds (Binette et al. 1996), standard power-law photoionisation models, and shock models (Dopita & Sutherland 1996), are shown in Fig. 19, together with the $[\text{Ne V}]/[\text{Ne III}]$ and $[\text{O II}]/[\text{O III}]$ line ratios measured for the galaxies in the

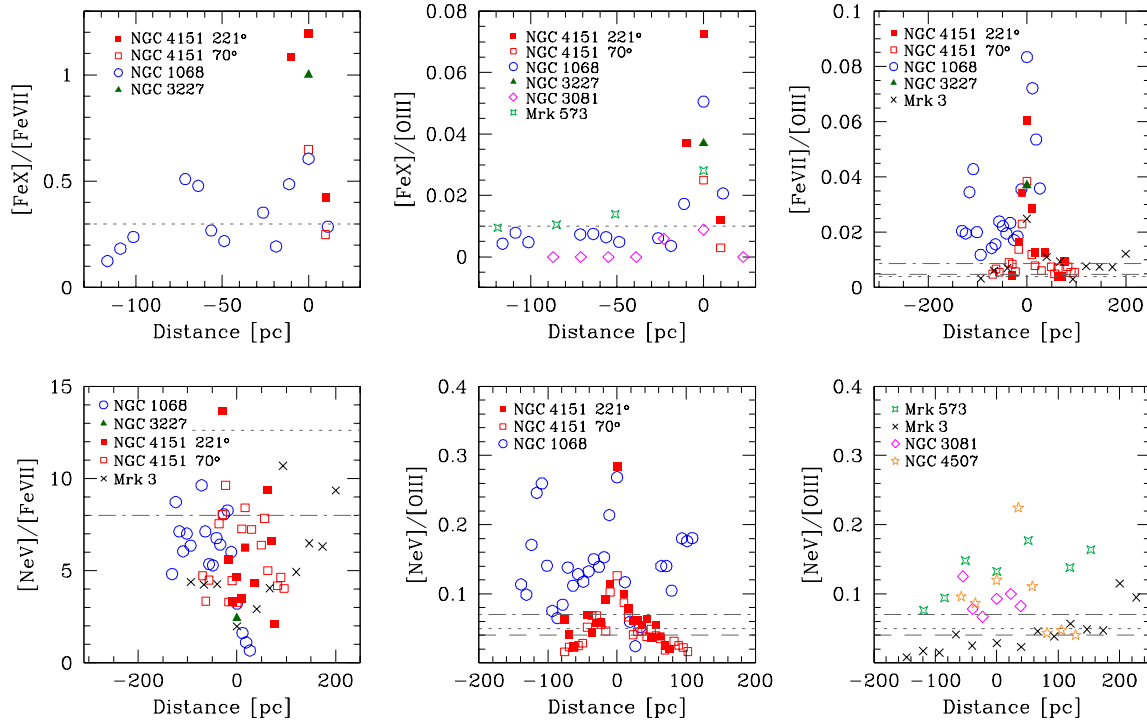


Figure 21. Coronal emission-line ratios measured for the galaxies in the sample as a function of the distance to the nucleus. Dotted lines correspond to the predictions of Ferguson et al. (1997a) models. Dot-dashed and dashed lines correspond to the BB20 and PB50 models of Komossa & Schulz (1997), respectively. Notice that, for visualisation purposes, we splitted the sample of galaxies when plotting the $[\text{NeV}]/[\text{OIII}]$ ratio.

sample. We have included the line ratios of NGC 4151, NGC 1068, and Mrk 3 for comparison purposes, but notice that these lines have already been modeled by Nelson et al. (2000), Kraemer et al. (2000), Collins et al. (2005, 2009), and Kraemer & Crenshaw (2000a). The models included in Fig. 19 were taken from fig. 4 of Tadhunter (2002). We also included a fiducial point from the dust-free models of Ferguson et al. (1997a) and those corresponding to the PB50 and BB20 models of Komossa & Schulz (1997). These multi-component models are described in more detail below. Note that the photoionisation models shown in Fig. 19 do not aim at a detailed modelling of every single emission line, like $[\text{NeV}]$, of every galaxy, but rather at presenting global trends. From this diagnostic diagram we can see that the photoionisation models of Ferguson et al. (1997a) and Komossa & Schulz (1997) reproduce the bulk of the line ratios fairly well. However, in some cases (e.g., Mrk 573 and NGC 1068) they underpredict the $[\text{NeV}]/[\text{NeIII}]$ ratio. In a small parameter space, the shock plus precursor and photoionisation models overlap, and within a very narrow parameter space shock plus precursor models also match the data (Mrk 3, NGC 4151, and NGC 7682); while the bulk of these particular models are off-set from the data - they systematically overpredict $[\text{OII}]/[\text{OIII}]$ and underpredict $[\text{NeIII}]/[\text{NeV}]$. A similar result was obtained by Nelson et al. 2000 for NGC 4151. Both, the pure shock models and the models including matter-bounded clouds overestimate the $[\text{OII}]/[\text{OIII}]$ line ratios, giving a poor description of the measured ratios in these galaxies. Although the line ratios

presented here were not corrected for extinction, an extreme correction would be required for the $[\text{OII}]/[\text{OIII}]$ intrinsic ratio to lie in the regions predicted by these models.

It is interesting to note that the line ratios from these galaxies do not vary very much, neither from galaxy to galaxy nor within each object, occupying a small zone in the diagrams. This can be better seen in Fig. 20, where we plot the $[\text{NeIII}]/[\text{NeV}]$ and $[\text{OII}]/[\text{OIII}]$ ratios as a function of the distance to the nucleus of the galaxies. For most of the objects in our sample these ratios do not vary strongly with the distance and show very similar values. Since these ratios are usually interpreted as a measure of the ionisation parameter (e.g., Penston et al. 1990; Komossa & Schulz 1997), their constancy would imply that the gas density in these galaxies decreases proportional to the square of the distance. Extra information concerning the extinction affecting the gas can be derived from these plots. As it was mentioned above, the line ratios were not corrected for extinction. However, the closeness in wavelength between the $[\text{NeV}]$ and $[\text{NeIII}]$ lines makes its ratio almost independent of reddening. On the other hand, the $[\text{OII}]/[\text{OIII}]$ ratio is more affected by dust extinction. We can see in Fig. 20 that, in most cases, both ratios show a very similar behaviour with respect to the distance to the nucleus, suggesting that the emission-line gas is not strongly affected by dust extinction.

Next, we focus on just the CLs for which not all models shown in Fig. 19 are available. Given large uncertainties in the collision strengths of the iron coronal lines (see, especially, the cautious comments by Ferguson et al. 1997a),

we limit any comparison between data and models to order of magnitude estimates. Ferguson et al. (1997b) carried out photoionisation calculations to identify the optimal conditions and locations in which the coronal lines form. Assuming that radiation from the central AGN is the only excitation mechanism, and using plane-parallel, constant density slabs of gas, they determined the distances from the ionising source in which the coronal lines are emitted as a function of density. They provide line equivalent widths in the density-distance plane, indicating where the bulk of the emission occurs for each line, and allowing rough comparisons between observed and predicted emission-line flux ratios. The [Ne v], [Fe VII], [Fe X], [Fe XI] and [Fe XIV] lines observed here are included in their calculations. They assumed an ionising EUV continuum similar to that of a typical Seyfert galaxy, with $L_{\text{ion}} = 10^{43.5}$ erg s $^{-1}$, where L_{ion} is the ionising luminosity of the central source. These models predict that, under optimal conditions³, the radius of the region emitting the [Ne v] and [Fe VII] lines is between 0.4–130 pc and 0.6–100 pc, respectively. For [Fe X], they show that it is restricted to the inner 20 pc while for [Fe XI] the emission region is not larger than one parsec. These values agree with the size of the CLRs derived in this work in all objects but Mrk 3, NGC 1068, and Mrk 573, where moderate to large discrepancies are found. In the former, both Fe $^{+6}$ and Ne $^{+4}$ extend to distances of about 200 pc. For the latter two objects, the greatest discrepancy is for the lines of high IP, that is, [Fe X] and [Fe XI], which are detected to scales of ~ 100 pc and 60 pc, respectively. For NGC 1068, Pier et al. (1994) and Bland-Hawthorn et al. (1997) estimate ionising luminosities 1–2 orders of magnitude higher than used by Ferguson et al. (1997b). If we take into account that the size of the emission region scales as $L_{\text{ion}}^{1/2}$, adopting $L_{\text{ion}} = 10^{45}$ erg s $^{-1}$ and leaving the other parameters of the model constant, the sizes of the emission regions for the different lines are increased by a factor of up to 4. The size of the region emitting [Fe X] is now in good agreement, but we now overestimate the size of the [Fe VII] region, which should now be visible to scales of several hundred parsecs. Furthermore, the region emitting [Fe XI] continues to be strongly underestimated. A similar argument can be applied to Mrk 573, although in that source the region containing [Fe XI] was not covered by STIS.

From a large grid of photoionisation models⁴, and assuming a “locally optimally emitting clouds” (LOC) scenario, Ferguson et al. (1997a) predicted integrated spectra for different distributions of cloud covering fraction and density. The integrated spectrum that best reproduces the [O II]/[O III] and [O III]/H β ratios of a mean Seyfert 2 spectrum also predicts [Fe X]/[Fe VII] and [Ne v]/[Fe VII] ratios of 0.3 and 12.6, respectively. These values can be compared with the ones measured in the galaxies of the sample, although keeping in mind that Ferguson et al.’s values are integrated over the whole NLR. The upper-left panel of Fig. 21 shows the distribution of the [Fe X]/[Fe VII] line ra-

tio found in NGC 1068, NGC 4151, and NGC 3227; the only galaxies where it could be measured. This ratio varies from about 0.1–1.2, with the largest values found at the nuclear positions. In the lower-left panel of Fig. 21 we show the [Ne v]/[Fe VII] ratio, which varies from about 1–15. Additionally, we included in Fig. 21 the ratios of the CLs over [O III]. In general, the line ratios tend to be higher at the nuclear positions, where the bulk of the CLs are emitted. We also added in Fig. 21 the predicted ratios from the photoionisation models of Komossa & Schulz (1997). Among their multi-component models, we representatively show two. These were computed for a mixture of gas densities and radii, varying the ionising EUV continuum: one continuum represented by a blackbody with $T = 200000$ K (BB20; for comparison purposes) and the other was described by a combination of a power law ($\alpha_{\text{UV-X}} = -2$) and BB20, each contributing 50% (PB50). It can be seen that the models of both, Ferguson et al. (1997a) and Komossa & Schulz (1997), do a relatively good job in reproducing the observed ratios, although they tend to underpredict the CLs measured at the most central regions of the galaxies. This is naturally expected, since the models included a mix over a range of radii, while at the smallest nuclear distances the highest ionisation lines are enhanced relative to the lower ionisation lines. Especially, given their high critical densities, coronal lines can be selectively boosted when adding a high-density component (e.g., table 3 of Komossa & Bade 1999). Excluding the nuclear regions, models and observations typically agree within a factor of a few. Since CLs sensitively depend on the EUV-SED, employing higher-temperature EUV bump components will naturally increase the strengths of the CLs with respect to the most lower ionisation lines (Komossa & Schulz 1997). Keeping further in mind the possibility of a contribution of matter-bounded clouds (which have a relatively smaller contribution from low-ionisation lines; e.g., Binette et al. 1997, Binette 1998) and the remaining uncertainties in the collisional strengths of the iron CLs (e.g., Ferguson et al. 1997b), we conclude that the consistency between photoionisation models and observations is gratifying.

In summary, the observational evidence presented in this section shows that photoionisation by a central source can account remarkably well for most of the coronal and low-ionisation line ratios measured in the galaxies of the sample.

5.3 Extinction: the case of NGC 1068

Several lines of evidence suggest that strong extinction, at distances towards the SW of the nucleus of NGC 1068, is playing an important role in the shape of its NLR: optical and NIR emission lines and continuum emission are weaker towards the SW (e.g., Machetto et al. 1994; Kraemer & Crenshaw 2000a; Thompson et al. 2001; Geballe et al. 2009); polarised light in the NIR towards the SW from the nucleus is not visible at optical wavelengths (Packham et al. 1997); and the silicate optical depth is strongly asymmetric, with a maximum at SSW position from the nucleus (Mason et al. 2006).

The STIS observations analysed here also points to strong extinction affecting the emission at SW distances from the nucleus (see Section 3.2). A close examination of Fig. 3 shows that toward the SW most CLs are suppressed, [Ne v] being the only one that can be observed at some posi-

³ $\log U(\text{H}) = -1.25, -2, -0.5, 0$ and range of $\log n(\text{H}) = 2.0-7.0, 3.0-7.5, 3.0-8.25, 5.0-6.5$ for [Ne v], [Fe VII], [Fe X], and [Fe XI], respectively.

⁴ With the same assumptions as in the Ferguson et al. (1997b) models, but the collision strengths of the iron transitions were set to 1 due to the large uncertainties in these quantities.

tions in that direction. Only [O III], the brightest of all optical lines, is visible at all apertures but its strength, compared to that of the NE side, is strongly suppressed, by up to a factor of 10. This suggests that indeed, strong extinction is present to the SW. The nucleus itself seems to be strongly attenuated too, as can be observed from the distribution of the ratio [Ne V]/[Fe VII] along the spatial direction measured in NGC 1068 shown in Fig. 21. This ratio is strongly sensitive to reddening because of the large difference in wavelength of the lines involved. It is independent of the form of the ionising continuum and likely of chemical abundances (except if metallicity shows a strong gradient along the slit). Fig. 21 shows that from about 20 pc NE of the nucleus and outwards, the ratio [Ne V]/[Fe VII] is relatively constant, with an average value of 7 ± 2 . In contrast, from 20 pc NE to the SW, it drops sharply, reaching 0.5 at only 25 pc to the SW. Moreover, Fig. 3 tells us that [Ne V] follows exactly the same spatial distribution as [O III]. No [Ne V] is detected at 50 pc SW, where a minimum in the [O III] distribution is observed. A few positions outwards, where the [O III] emission increases again, [Ne V] also does, becoming visible up to ~ 120 pc, where it is no longer detected. Note that to the NE, the maximum distance where we detect [Ne V] is 140 pc. We therefore confirm that the size of the [Ne V] emission region measured to the NE is very similar to that towards the SW. We conclude, therefore, that it is the strong extinction to the SW that blocks the detection of CLs in this direction. Note that the dust blocking the coronal lines is not spatially uniform. Rodríguez-Ardila et al. (2006) report the detection of [Fe VII] up to 120 pc south of the nucleus. In their observations, these authors employed a $1''$ slit aligned in the North-South direction.

It calls the attention that the coronal lines that seem to be strongly extinguished along the STIS slit in NGC 1068 are those coming from ions that are usually locked up into grains: iron and silicon. Therefore, in summary, dust extinction, and the gas phase depletion of refractory elements, very plausibly explain the observations of NGC 1068.

6 SUMMARY AND CONCLUSIONS

We have presented a study of the CLR of a sample of ten Seyfert galaxies based on optical STIS/HST spectra. These spectra allowed us to resolve the regions emitting CLs, and to analyse the properties of the CLs as a function of the distance to the nucleus. Our main results can be summarised as follows:

(i) CLs display very similar flux distributions than low-ionisation lines, showing a clumpy morphology. The CLRs extent from less than 10 pc up to 230 pc in radius; the most compact one is observed in NGC 3227, the most extended one in Mrk 3. We confirm, that high-ionisation CLs arise from more compact regions than the lower ionisation CLs. The compactness of the CLR is consistent with an origin of the bulk of the CLs between BLR and NLR, and extending well into the NLR (up to 100s of pc) in [Fe VII] and [Ne V]. Moreover, the distribution of the ratios between CLs and [O III] shows its maximum at the nucleus.

(ii) The two (ionisation-parameter sensitive) line ratios, [O II]/[O III] and [Ne III]/[Ne V], generally show very similar radial dependencies.

(iii) The highest ionisation CLRs appear to be the ones in NGC 4151 and NGC 3227, in terms of the [Fe X]/[Fe VII] line ratio. However, only in NGC 1068 we observed [Si XII], the highest ionisation line observed in the galaxies of the sample.

(iv) In general, the CL profiles show strong asymmetries, that vary with the distance to the nucleus. In some cases we observe line splitting in the core, sometimes locally complex with several components contributing. In particular, a remarkable double-peak structure was observed in the [Fe X] lines of Mrk 573 and NGC 4507. In the case of Mrk 573, the relative separation between the two peaks increases when going from NW to SE. This signals the presence of a highly energetic outflow, not detected in lower ionisation lines.

(v) Patterns of rotation curves in [O III] are generally followed by CLs. Local deviations occur, occasionally. Maximal ΔV of CLs reach up to typically 500 km s^{-1} (1000 km s^{-1} in case of NGC 1068) with both, red- and blueshifts occurring. Variation in width and peak position of the lines occurs from point to point without any particular universal trend with respect to the IP of the lines.

(vi) The presence or absence of CLs, their strengths, and kinematics, does not scale in any obvious and strong way with the radio properties (position of radio knots in jets).

(vii) Several lines of evidence point towards photoionisation as major ionisation mechanism: the generally close spatial dependencies between CLs and low-ionisation lines, the low inferred gas temperatures of order 10000–20000 K typical of photoionised gas, and the fact that available photoionisation models are generally successful in matching observed line ratios, within a factor of a few.

Our work demonstrated the power of spatially resolved spectroscopy to provide information of the inner parts of AGNs, where the bulk of CLs arise. A full comprehension of these lines is very important in order to improve our knowledge about energetic processes, such as outflows and shocks, occurring in the very galaxy cores.

ACKNOWLEDGMENTS

XM acknowledges scholarships from the Deutscher Akademischer Austausch Dienst (DAAD) and from the Consejo Nacional de Investigaciones Científicas y Técnicas (CONICET). A.R.A acknowledges support of the Brazilian Funding Agency CNPq under grant 311476/2006-6.

REFERENCES

- Antonucci R., Hurt T., Miller J., 1994, *ApJ*, 430, 210
- Appenzeller, I., Östreicher, R., 1988, *AJ*, 95, 45
- Arp H., 1966, *ApJS*, 14, 1
- Axon, D. J., Marconi, A., Capetti, A., Maccetto, F. D., Schreier, E., Robinson, A., 1998, *ApJ*, 496L, 75
- Bedregal A. G., Colina L., Alonso-Herrero A., Arribas S., 2009, *ApJ*, 698, 1852
- Best P. N., Röttgering H. J. A., Lehnert M. D., 1999, *MNRAS*, 310, 223
- Binette L., 1998, *MNRAS*, 294L, 47
- Binette L., Wilson A. S., Storchi-Bergmann T., 1996, *A&A*, 312, 365

- Binette L., Wilson A. S., Raga A., Storchi-Bergmann T., 1997, *A&A*, 327, 909
- Bland-Hawthorn J., Lumsden S. L., Voit G. M., Cecil G. N., Weisheit J. C., 1997, *Ap&SS*, 248, 177
- Brandt W. N., Pounds K., Fink H. H., 1995, *MNRAS*, 273, L47
- Brodie J., Willick J. A., Bowyer S., Henry J. P., 1987, *AJ*, 93, 1054
- Buta R., 1990, *ApJ*, 351, 62
- Capetti A., Axon D. J., Macchetto F., Sparks W. B., Boksenberg A., 1996, *ApJ*, 469, 554
- Capetti A., Macchetto F., Axon D. J., Sparks W. B., Boksenberg A., 1995, *ApJ*, 448, 600
- Capetti A., Axon D. J., Macchetto F. D., Marconi A., Winge C., 1999, *ApJ*, 516, 187
- Collins N. R., Kraemer S. B., Crenshaw D. M., Ruiz J., Deo R., Bruhweiler F. C., 2005, *ApJ*, 619, 116
- Collins N. R., Kraemer S. B., Crenshaw D. M., Bruhweiler F. C., Melndez M., 2009, *ApJ*, 694, 765
- Contini M., Viegas S. M., 2001, *ApJS*, 132, 211
- Cooke B. A., Elvis M., Ward M. J., Fosbury R. A. E., Penston M. V., Maccacaro T., 1976, *MNRAS*, 177P, 121
- Crenshaw D. M., Kraemer S. B., 2000, *ApJ*, 532L, 101
- Crenshaw D. M., Kraemer S. B., Hutchings J. B. et al., 2000, *AJ*, 120, 1731
- Cruz-González I., Carrasco L., Serrano A., Guichard J., Dultzin-Hacyan D., Bisiacchi G. F., 1994, *ApJS*, 94, 47
- Das V., Crenshaw D. M., Kraemer S. B., Deo R. P., 2006, *AJ*, 132, 620
- Deo R. P., Crenshaw D. M., Kraemer S. B., Dietrich M., Elitzur M., Teplitz H., Turner T. J., 2007, *ApJ*, 671, 124
- De Robertis M. M., Osterbrock D. E., 1984, *ApJ*, 286, 171
- De Robertis M. M., Shaw R. A., 1990, *ApJ*, 348, 421
- Dopita M. A., Sutherland R. S., 1995, *ApJ*, 455, 468
- Dopita M. A., Sutherland R. S., 1996, *ApJS*, 102, 161
- Durret F., 1994, *A&AS*, 105, 57
- Durret F., Bergeron J., 1986, *A&A*, 156, 51
- Evans I. N., 1988, *ApJS*, 67, 373
- Evans I. N., Ford H. C., Kinney A. L., Antonucci R. R. J., Armus L., Caganoff S., 1991, *ApJ*, 369L, 27
- Erkens U., Appenzeller I., Wagner S., 1997, *A&A*, 323, 707
- Falcke H., Wilson A. S., Simpson C., 1998, *ApJ*, 502, 199
- Fath E.A., 1909, *LicOB*, 5, 71
- Ferguson J. W., Korista K. T., Baldwin J. A., Ferland G. J., 1997a, *ApJ*, 487, 122
- Ferguson J. W., Korista K. T., Ferland G. J., 1997b, *ApJS*, 110, 287
- Ferruit P., Wilson A. S., Falcke H., Simpson C., Pcontal E., Durret F., 1999, *MNRAS*, 309, 1
- Gallimore J. F., Baum S. A., O'Dea C. P., Pedlar A., 1996, *ApJ*, 458, 136
- Geballe T. R., Mason R. E., Rodríguez-Ardila A., Axon D. J., 2009, *ApJ*, 701, 1710
- Gelbord J. M., Mullaney J. R., Ward M. J., 2009, *MNRAS*, 397, 172
- Gorjian V., Cleary K., Werner M. W., Lawrence C. R., 2007, *ApJ*, 655L, 73
- Grandi S. A., 1978, *ApJ*, 221, 501
- Grupe D., Beuermann K., Mannheim K., Bade N., Thomas H.-C., de Martino D., Schwobe A., 1995, *A&A*, 299, L5
- Haniff C. A., Wilson, A. S., Ward M. J., 1988, *ApJ*, 334, 104
- Heisler C. A., De Robertis M. M., 1999, *AJ*, 118, 2038
- Holt J., Tadhunter C. N., Morganti R., 2006, *AN*, 327, 147
- Huchra J., Burg R., 1992, *ApJ*, 393, 90
- Hutchings J. B., Crenshaw D. M., Kaiser M. E. et al., 1998, *ApJ*, 492L, 115
- Hutchings J. B., Crenshaw D. M., Danks A. C. et al., 1999, *AJ*, 118, 2101
- Imanishi M., Alonso-Herrero A., 2004, *ApJ*, 614, 122
- Jaffe W., Balbi A., Bond J. R. et al., 2004, *Natur*, 429, 47
- Kaiser M. E., Bradley L. D. II, Hutchings J. B. et al., 1999, *Ap&SS*, 269, 431
- Keenan F. P., Norrington P. H., 1987, *A&A*, 181, 370
- Kinkhabwala A., Sako M., Behar E. et al., 2002, *ApJ*, 575, 732
- Knop R. A., Armus L., Matthews K., Murphy T. W., Soifer B. T., 2001, *AJ*, 122, 764
- Komossa S., Bade N., 1999, *A&A*, 343, 775
- Komossa S., Fink H., 1997a, *A&A*, 322, 719
- Komossa S., Fink H., 1997b, *A&A*, 327, 483
- Komossa S., Schulz H., 1997, *A&A*, 323, 31
- Komossa S., Xu D., Zhou H., Storchi-Bergmann T., Binette L., 2008, *ApJ*, 680, 926
- Komossa S., Zhou H., Rau A. et al., 2009, *ApJ*, 701, 105
- Korista K. T., Ferland G. J., 1989, *ApJ*, 343, 678
- Koski A. T., 1978, *ApJ*, 223, 56
- Kraemer S. B., Crenshaw D. M., 2000b, *ApJ*, 532, 256
- Kraemer S. B., Crenshaw D. M., 2000a, *ApJ*, 544, 763
- Kraemer S. B., Trippe M. L., Crenshaw D. M., Meléndez M., Schmitt H. R., Fischer T. C., 2009, *ApJ*, 698, 106
- Kukula M. J., Ghosh T., Pedlar A., Schilizzi R. T., Miley G. K., de Bruyn A. G., Saikia D. J., 1993, *MNRAS*, 264, 893
- Kukula M. J., Ghosh T., Pedlar A., Schilizzi R. T., 1999, *ApJ*, 518, 117
- Lutz D., Maiolino R., Moorwood A. F. M., Netzer H., Wagner S. J., Sturm E., Genzel R., 2002, *A&A*, 396, 439
- Macchetto F., Capetti A., Sparks W. B., Axon D. J., Boksenberg A., 1994, *ApJ*, 435L, 15
- Malkan M. A., 1986, *ApJ*, 310, 679
- Marconi A., Moorwood A. F. M., Salvati M., Oliva E., 1994, *A&A*, 291, 18
- Marconi A., van der Werf P. P., Moorwood A. F. M., Oliva E., 1996, *A&A*, 315, 335
- Mason R. E., Geballe T. R., Packham C., Levenson N. A., Elitzur M., Fisher R. S., Perlman E., 2006, *ApJ*, 640, 612
- Miller J. S., Goodrich R. W., 1990, *ApJ*, 355, 456
- Miller J. S., Goodrich R. W., Mathews W. G., 1991, *ApJ*, 378, 47
- Moran E. C., Barth A. J., Kay L. E., Filippenko A. V., 2000, *ApJ*, 540L, 73
- Morris S., Ward M., Whittle M., Wilson A. S., Taylor K., 1985, *MNRAS*, 216, 193
- Morris S. L., Ward M. J., 1988, *MNRAS*, 230, 639
- Morse J. A., Raymond J. C., Wilson A. S., 1996, *PASP*, 108, 426
- Mullaney J. R., Ward M. J., 2008, *MNRAS*, 385, 53
- Mullaney J. R., Ward M. J., Done C., Ferland G. J., Schurch N., 2009, *MNRAS*, 394L, 16
- Mundell C. G., Holloway A. J., Pedlar A., Meabur J., Kukula M. J., Axon D. J., 1995, *MNRAS*, 275, 67
- Nagao T., Murayama T., Shioya Y., Taniguchi Y., 2003, *AJ*, 125, 1729

- Nagao T., Taniguchi Y., Murayama T., 2000, *AJ*, 119, 2605
- Nagao T., Kawabata K. S., Murayama T., Ohyama Y., Taniguchi Y., Shioya Y., Sumiya R., Sasaki S. S., 2004, *AJ*, 128, 2066
- Nagar N. M., Wilson A. S., Mulchaey J. S., Gallimore J. F., 1999, *ApJS*, 120, 209
- Neff S. G., de Bruyn A. G., 1983, *A&A*, 128, 318
- Nelson C. H., Weistrop D., Hutchings J. B., Crenshaw D. M., Gull T. R., Kaiser M. E., Kraemer S. B., Lindler D., 2000, *ApJ*, 531, 257
- Netzer H., 1974, *MNRAS*, 169, 579
- Ogle P. M., Marshall H. L., Lee J. C., Canizares C. R., 2000, *ApJ*, 545L, 81
- Oliva E., Moorwood A. F. M., 1990, *ApJ*, 348L, 5
- Oliva E., Salvati M., Moorwood A. F. M., Marconi A., 1994, *A&A*, 288, 457
- Osterbrock D. E., 1989, *Astrophysics of Gaseous Nebulae and Active Galactic Nuclei*, University Science Books, Mill Valley, CA
- Osterbrock D. E., Shaw R. A., Veilleux S., 1990, *ApJ*, 352, 561
- Packham C., Young S., Hough J. H., Axon D. J., Bailey J. A., 1997, *MNRAS*, 288, 375
- Pelat D., Alloin D., Fosbury R. A. E., 1981, *MNRAS*, 195, 787
- Penston M. V., Fosbury R. A. E., Bokserberg A., Ward M. J., Wilson A. S., 1984, *MNRAS*, 208, 347
- Penston M., Robinson A., Alloin D. et al., 1990, *A&A*, 236, 53
- Pérez E., Gonzalez-Delgado R., Tadhunter C., Tsvetanov Z., 1989, *MNRAS*, 241P, 31
- Pier E. A., Antonucci R., Hurt T., Kriss G., Krolik J., 1994, *ApJ*, 428, 124
- Pier E. A., Voit G. M., 1995, *ApJ*, 450, 628
- Phillips M. M., Osterbrock D. E., 1975, *PASP*, 87, 949
- Pogge R. W., 1989, *ApJ*, 345, 730
- Pogge R. W., De Robertis M. M., 1993, *ApJ*, 404, 563
- Pogge R. W., De Robertis M. M., 1995, *ApJ*, 451, 585
- Pogge R. W., Martini P., 2002, *ApJ*, 569, 624
- Pogge R. W., Owen J. M., 1993, OSU Internal Report 93-01
- Porquet D., Dumont A.-M., Collin S., Mouchet M., 1999, *A&A*, 341, 58
- Pounds K. A., Page K. L., 2005, *MNRAS*, 360, 1123
- Prieto A. M., Marco O., Gallimore J., 2005, *MNRAS*, 364L, 28
- Prieto M. A., Meisenheimer K., Marco, O. et al., 2004, *ApJ*, 614, 135
- Quillen A. C., Alonso-Herrero A., Rieke M. J., McDonald C., Falcke H., Rieke G. H., 1999, *ApJ*, 525, 685
- Ramos Almeida C., Pérez García A. M., Acosta-Pulido J. A., González-Martín O., 2008, *ApJ*, 680L, 17
- Regan M. W., Mulchaey J. S., 1999, *AJ*, 117, 2676
- Reunanen J., Kotilainen J. K., Prieto M. A., 2003, *MNRAS*, 343, 192
- Riffel R., Pastoriza M. G., Rodríguez-Ardila A., Maraston C., 2007, *ApJ*, 659L, 103
- Riffel R., Rodríguez-Ardila A., Pastoriza M. G., 2006, *A&A*, 457, 61
- Riffel R. A., Storchi-Bergmann T., Winge C., McGregor P. J., Beck T., Schmitt H., 2008, *MNRAS*, 385, 1129
- Rodríguez-Ardila A., Prieto M. A., Viegas S., Gruenwald R., 2006, *ApJ*, 653, 1098
- Rodríguez-Ardila A., Viegas S. M., Pastoriza M. G., Prato L., 2002, *ApJ*, 579, 214
- Ruiz J. R., Crenshaw D. M., Kraemer S. B., Bower G. A., Gull T. R., Hutchings J. B., Kaiser M. E., Weistrop D. et al., 2001, *AJ*, 122, 2961
- Ruiz, J. R., Crenshaw D. M., Kraemer S. B., Bower G. A., Gull T. R., Hutchings J. B., Kaiser M. E., Weistrop D., 2005, *AJ*, 129, 73
- Sako M., Kahn S. M., Paerels F., Liedahl D. A., 2000, *ApJ*, 543L, 115
- Sánchez F. M., Davies R. I., Eisenhauer F., Tacconi L. J., Genzel R., Sternberg, A., 2006, *A&A*, 454, 481
- Schlesinger K., Pogge R. W., Martini P., Shields J. C., Fields D., 2009, *ApJ*, 699, 857
- Schmitt H. R., Storchi-Bergmann T., Baldwin J. A., 1994, *ApJ*, 423, 237
- Schmitt H. R., Donley J. L., Antonucci R. R. J., Hutchings J. B., Kinney A. L., 2003, *ApJS*, 148, 327
- Schulz H., 1988, *A&A*, 203, 233
- Schulz H., 1995, *Habilitationsschrift*, Ruhr-Universität Bochum
- Seyfert C. K., 1943, *ApJ*, 97, 28
- Simpson C., Wilson A. S., Bower G., Heckman T. M., Krolik J. H., Miley G. K., 1997, *ApJ*, 474, 121
- Spinelli P. F., Storchi-Bergmann T., Brandt C. H., Calzetti D., 2006, *ApJS*, 166, 498
- Steffen W., Gomez J. L., Williams R. J. R., Raga A. C., Pedlar A., 1997, *MNRAS*, 286, 1032
- Storchi-Bermann T., McGregor P. J., Riffel R. A., Simões Lopes R., Beck T., Dopita M., 2009, *MNRAS*, 394, 1148
- Storchi-Bergmann T., Wilson A. S., Mulchaey J. S., Binette L., 1996, *A&A*, 312, 357
- Sturm E., Alexander T., Lutz D., Sternberg A., Netzer H., Genzel, R., 1997, *ApJ*, 512, 197
- Sturm E., Lutz D., Verma A., Netzer H., Sternberg A., Moorwood A. F. M., Oliva E., Genzel R., 2002, *A&A*, 393, 821
- Tadhunter C. N., 2002, *RMxAC*, 13, 213
- Tadhunter C. N., Fosbury R. A. E., di Serego Alighieri S., Bland J., Danziger I. J., Goss W. M., McAdam W. B., Sniijders M. A. J., 1988, *MNRAS*, 235, 403
- Taylor D., Dyson J. E., Axon D. J., 1992, *MNRAS*, 255, 351
- Thompson R. I., Chary Ranga-Ram, Corbin M. R., Epps H., 2001, *ApJ*, 558L, 97
- Tsvetanov Z., Walsh J. R., 1992, *ApJ*, 386, 485
- Ulrich M. H., 1973, *ApJ*, 181, 51
- Ulrich M. H., 2000, *A&ARv*, 10, 135
- Ulvestad J. S., Wilson A. S., 1989, *ApJ*, 343, 659
- Ulvestad J. S., Wilson A. S., Sramek R. A., 1981, *ApJ*, 247, 419
- Veilleux S., 1988, *AJ*, 95, 1695
- Veron-Cetty M. P., Veron P., 1998, *A Catalogue of Quasars and Active Nuclei*, ESO Sci Rep. 18 (8th ed. ; Garching: ESO)
- Viegas-Aldrovandi S. M., Contini M., 1989, *A&A*, 215, 253
- Ward M., Morris S., 1984, *MNRAS*, 207, 867
- Whittle M., Rosario D. J., Silverman J. D., Nelson C. H., Wilson A. S., 2005, *AJ*, 129, 104
- Wilson A. S., 1979, *RSPSA*, 366, 461
- Wilson A. S., Nath B., 1990, *ApJS*, 74, 731
- Wilson A. S., Ulvestad J. S., 1983, *ApJ*, 275, 8

Winge C., Axon D. J., Macchetto F. D., Capetti A., 1997,
ApJ, 487L, 121
Young S., Hough J. H., Axon D. J., Bailey J. A., Ward M.
J., 1995, MNRAS, 272, 513
Young A. J., Wilson A. S., Shopbell P. L., 2001, ApJ, 556,
6